4-2015

Comparing Different Methods for Estimating Total Open Heliospheric Magnetic Flux

Samantha J. Wallace

COMPARING DIFFERENT METHODS FOR ESTIMATING TOTAL OPEN HELIOSPHERIC MAGNETIC FLUX

BY
SAMANTHA J. WALLACE

A Thesis
Submitted to the Department of Physical Sciences
and the Committee on Graduate Studies
In partial fulfillment of the requirements
for the degree of
Master in Science in Engineering Physics

April 2015
Embry-Riddle Aeronautical University
Daytona Beach, Florida

COMPARING DIFFERENT METHODS FOR ESTIMATING TOTAL OPEN HELIOSPHERIC MAGNETIC FLUX

by

Samantha J. Wallace

This thesis was prepared under the direction of the candidate's Thesis Committee Chair, Dr. John Hughes, Associate Professor, Daytona Beach Campus, and Thesis Committee Members Dr. Katariina Nykyri, Associate Professor, Daytona Beach Campus and Dr. Matthew Zettergren, Assistant Professor, Daytona Beach Campus, and has been approved by the Thesis Committee. It was submitted to the Department of Physical Sciences in partial fulfillment of the requirements for the degree of Master of Science in Engineering Physics

THESIS COMMITTEE:

Dr. John Hughes,
Committee Chair

Dr. Charles N. Arge,
Committee Member

Dr. Katariina Nykyri,
Committee Member

Dr. Matthew Zettergren,
Committee Member

Dr. Peter Erdman,
Graduated Program Chair,
Engineering Physics

Dr. Terry Oswalt,
Department Chair,
Physical Sciences

Dr. William Grams,
Dean, College of Arts and Sciences

Dr. Robert Oxley,
Associate V.P. for Academics

Nomenclature

ACE	Advanced Composition Explorer
ADAPT	Air Force Data Assimilative Photospheric Flux Transport
AIA	Atmospheric Imaging Assembly
AU	Astronomical unit
$\mathbf{B}$	Magnetic field
$\mathbf{B}_r$	Radial component of the magnetic field
$\mathbf{B}_\theta$	Tangential component of the magnetic field
$\mathbf{B}_z$	z-component of the magnetic field
β	Plasma beta
CR	Carrington rotation
Closed Magnetic Field	A magnetic field line that has both endpoints rooted in the photosphere.
CME	Coronal Mass Ejection

dA	Differential area
Diachronic	Something as it has evolved over time
EUV	Extreme Ultraviolet
EUV	Extreme Ultraviolet Imager
EnLS	Ensemble Least Squares Method
FITS	Flexible Image Transport System
GGS	Global Geospace Science
GSE	Geocentric Solar Ecliptic
ISEE-3	International Sun/Earth Explorer 3
kG	Kilogauss
He	Helium
KPVT	Kitt Peak Vacuum Telescope
LANL	Los Alamos National Laboratory
MHD	Magnetohydrodynamics
MSFC	Marshall Space Flight Center
μ_0	Permeability of free space
nm	Nanometer
NOAA	National Oceanic and Atmospheric Administration
NSO	National Solar Observatory
LMSAL	Lockheed-Martin Solar and Astrophysics Laboratory

LR OMNI data	Low resolution, spacecraft interspersed, near Earth solar wind data
Open Magnetic Field	Magnetic field lines that do not connect back within the solar atmosphere, and presumably reconnect with an oppositely directed field in the interstellar medium.
PFSS	Potential Field Source Surface
p_{gas}	Gas pressure
Φ	Total magnetic flux
p_{mag}	Magnetic pressure
R	Heliocentric distance
$R_{\odot}$	Solar interior radius
SAO	Smithsonian Astrophysical Observatory
SCS	Schatten Current Sheet
SDO	Solar Dynamics Observatory
SECCHI	Sun Earth Connection Coronal and Heliospheric Investigation
SOLIS	Synoptic Optical Long-Term Investigations of the Sun
STEREO	Solar Terrestrial Relations Observatory
SWPC	Space Weather Prediction Center
Synchronic	Something as it exists at one point in time
UV	Ultraviolet
VSM	Vector Spectromagnetograph

WH	Worden & Harvey Model
WSA	Wang Sheeley Arge Model

Abstract

There are extended periods over the solar cycle where significant discrepancies occur between the observed open magnetic flux (i.e., those based on spacecraft observations) and that determined from coronal models. One explanation for the source of these discrepancies is the magnetic fields in CMEs, which have yet to magnetically disconnect from the Sun. These "closed" flux sources can be included in open flux estimates, because open and closed magnetic field lines are not easily distinguished in spacecraft data. Another possibility is that a portion of the open flux measured by in situ spacecraft originates from the time-dependent evolution of solar magnetic fields that is not captured by static or steady state coronal model solutions. In this research, the total open heliospheric magnetic flux is computed using three different methods and then compared with results obtained using in situ interplanetary magnetic field observations. The first two methods make use of the Potential Field Source Surface (PFSS) model to calculate the total open magnetic flux using as its input: 1) traditional Carrington or diachronic maps and 2) Air Force Data Assimilative Photospheric Flux Transport (ADAPT) model synchronic maps. The diachronic and synchronic photospheric magnetic field maps are derived from magnetograms from the same source, namely the National Solar Observatory (NSO) Kitt Peak Vacuum Telescope (KPVT) and Vector

Spectromagnetograph (VSM) magnetographs. The third method involves the use of observationally derived Helium and EUV coronal hole maps overlain on the above mentioned magnetic field maps to compute total open magnetic flux. The results of this work show that alternative approaches using observationally derived coronal holes to compute the open flux match well with what the model derives, especially near solar minimum. Both deviate from the spacecraft data especially near solar maximum. This suggests that the models are determining coronal hole boundaries well, but are unable to capture open flux resulting from the opening and closing of field lines during solar maximum. A primary suspicion also is that spacecraft instruments could be mistaking the field's tangential component for the radial component due to oscillations in the field lines. Future research will work to filter out the field's tangential component that could be causing inaccuracies in the observed radial field.

Acknowledgments

As I reflect on this work, I am unceasingly thankful to God first and foremost. This research is fruit and evidence of His redemptive work in my life. He has changed me from a broken, unmotivated, scattered youth to a diligent, aware, and empathetic adult in my pursuit of knowing Him above all else.

In all honesty, there are an overwhelming number of people that deserve much thanking. As I meditate on that, I am overjoyed and thankful for all these rich relationships. God has never led me somewhere where that wasn't the defining factor. That being said, I would like to thank Ben Wallace, for loving me with God's heart, encouraging me, and living out the day to day of this process with me. He has been patient and kind, and has constantly showed me what love truly looks like toward others and myself.

There is one person on this Earth who I share many characteristics, qualities, and morals with that has established how I live my life. This person is my dad. Over the course of my life I have watched him pour out his life for not just my mom and us kids, but many people. I've also witnessed him reap the fruits of his labors. He is a living testimony of the importance of honesty and hard work above having a degree. He hasn't always been able to understand why his oldest child is STILL in school, but he has always supported my decisions and guided me along the way.

Equally, I would like to thank my mom and siblings. My mom has been there through all the tears, fears, changes, and challenges that I've faced. It was always nice to have a listening ear. Also, I know it has been difficult for my siblings for their big sister to go off and pursue her crazy dreams, and I thank them for always loving me through that. Further, I am forever grateful to Jeremy and Rachel Folmsbee, and their children who have become my brothers and sisters as well. It is not possible that I would have made it through my master's degree without their love, prayer, fellowship, counsel, encouragement, and hot meals. They have graciously invited me to live with them and be a part of their family for the past two and a half years. Their display of what it looks like to live like Christ, and their selflessness has affected me immensely.

I am sincerely thankful to Dr. Nick Arge, his wife Lisa, and his family. Nick has invested in my life as a mentor and has co-advised this research. He has a teacher's heart, and has worked over the past three years to launch my graduate academic career. I hope to advise a student with his caring attitude and enthusiasm for research someday. Likewise, Dr. John Hughes has mentored me and co-advised this research. He leads by example and displays what it means to "take time" in life, whether that is with advising students or leaving work at work to be with family. I am thankful for his mentorship throughout my academic career.

I would not be here today without the people that God has placed at the beginnings and ends of chapters in my life. Every person is uniquely, but equally valuable. They have all held a certain role without which none of this would be possible. Lastly, I am grateful for all the unmentioned friends and extended family for the infinite amount of laughter and love. If there is one thing I learned from this process, it is that self-sacrificial love to and from others is the key to overcoming life's challenges. The support and mentorship of others were crucial components to the completion of this work, and to the person I am today.

Contents

List of Figures

"Just imagine becoming the way you used to be as a very young child, before you understood the meaning of any word, before opinions took over your mind.
The real you is loving, joyful, and free.
The real you is just like a flower, just like the wind, just like the ocean,
... just like the Sun."

Miguel Angel Ruiz

Preface

The Sun fascinates all who ponder its majesty. It is faithful to rise and set, defining each day from the next. It is near, yet distant, quiet, yet brutally dynamic, life giving, yet full of fury. The Sun illuminates all that it touches, separating darkness from light. It does not ask for anything in return and does not discriminate when unfolding its radiance. Without the empty, vast, darkness of space, we would not know the beauty and unrestrained glory of the light.

The Sun has a lot to say, from its symbolic parallels to love and truth to the observations of stellar physical phenomena and how they affect our lives. The Sun is the key to unlocking the secrets of the astral universe. It's "so close we can touch it", through resolving its surface features and magnetic activity. This information provides insight for stellar models and calibrating observations of more distant stars. Discoveries such as helioseismology and magnetic activity cycles on the Sun have pointed scientists directly to the same processes occurring on other stars.

The Sun's significance doesn't end there. It provides almost all of our energy, from heat and weather, to fossil fuels and food. In addition, the Sun constantly interacts with the terrestrial environment. Variations in the Sun's magnetic field heavily affect the solar wind and disturbances of Earth's

magnetosphere. They result in aurorae, geomagnetic activity, and consequently, satellite malfunctioning and communication interference. It is imperative that we understand how and when the solar magnetic field fluctuates in order to prepare for such upheaval.

Despite its relative nearness to Earth, it is a challenging pursuit to study the Sun. Mathematically modeling its physical processes requires a mix of direct observation and intricate theory. For as far as we've come in grasping the mechanics of the Sun, there is a wealth of even fundamentals that are not altogether fully understood. This study presents results to contribute to the understanding and accurate determination of one facet of solar magnetic fields. It exploits both traditional and new methods for its derivation and compares results with in situ observations, while providing insight to model and observational shortcomings.

The potential in the future of solar physics is great, making this field of study very interesting. The Sun is tangible to our finite mind. It is a laboratory within reach to investigate physical phenomena not observable on Earth. Through its study we can better understand how it drives the terrestrial environment, and everything from birth to death and in between of a stars life.

Chapter 1: Background

1.1 The Solar Interior: Energy Generation and Transport

At the Sun's core, encompassing the first 25 percent of the Sun's radius, gravity pulls mass inward, creating a density of 151 x 10^3 kg/m^3. This allows enough gas pressure for the proton-proton chain reaction to fuse hydrogen atoms into the helium isotope ^{4}He. This reaction initiates the energy generation process for a celestial body about 330,000 times more massive than Earth. The difference of mass between He and H is converted to energy, seen in the high temperatures of the core, near 15 million K. Moving outward as electromagnetic radiation, photons transfer this energy to the radiation zone. Here, atoms encounter continuous scattering due to the highly dense, ionized plasma at temperatures near 5 million K. A photon travels only a few microns before the process beings again, taking on order of 10^{25} absorptions and re-emissions before their energy reaches the surface. Timescales of approximately 170 thousand years are estimated for energy to travel nearly half of the solar interior radius (.25 - .7 $R_\odot$) out of the radiation zone (Priest, 1995).

Beyond the radiation zone, the opacity is so high that energy flux cannot be transmitted as electromagnetic radiation. Cooler temperatures (2 million K) produce a steep temperature gradient, allowing heat to be trapped. This is how convection cells form and take over the energy transport process. The very thin transitional layer marking the change in rotation rate between these two strikingly different regions is the tachocline. The tachocline marks where the Sun changes from nearly solid body rotation ($< .7\ R_{\odot}$) to a differentially rotating body. A steep enough temperature gradient or a high heat capacity within the convection zone allows plasma to remain warmer and less dense than its surroundings even after expansion and cooling. Its buoyancy will then cause it to rise further, producing overturning convection cells and forming granulation, the dominant pattern of the quiet solar surface (Priest, 1995). The science of helioseismology allows solar physicists to study the solar interior through its natural oscillations, making it possible to understand these mechanisms.

1.2 The Solar Magnetic Field

The Sun is permeated by magnetic fields of varying strengths and spatial scales. Except during times of high solar activity (solar maximum), the Sun has large-scale concentrations of magnetic flux at each of its poles producing, to first order, a global dipole field. The upper solar atmosphere experiences high temperatures with a low density of plasma. In this region the magnetic field pressure dominates over the gas pressure resulting in the magnetic field being full fully coupled to the plasma. This observed "frozen-in" phenomena results in the solar material and embedded magnetic field moving together as one. This is how the Sun's magnetic field determines the structure and nature of the solar atmosphere.

1.2.1 Differential Rotation

The Sun rotates counterclockwise as viewed from north, tilted 7.25 degrees on axis perpendicular to the ecliptic plane. Tracking surface features moving left to right across disk center first revealed that an increase in absolute latitude corresponds with a decrease in rotation rate. The equatorial field lines are pulled faster ahead than at higher latitudes, resulting in the deformity of magnetic field lines depicted in Figure 1.1. This process is known as the omega (ω) effect, where the poloidal (meridional) component of the field is stretched in the toroidal (azimuthal) direction (Bushby & Mason, 2004). The ω-effect is the cause for many of the observed features within the solar atmosphere that will be discussed later in this chapter.

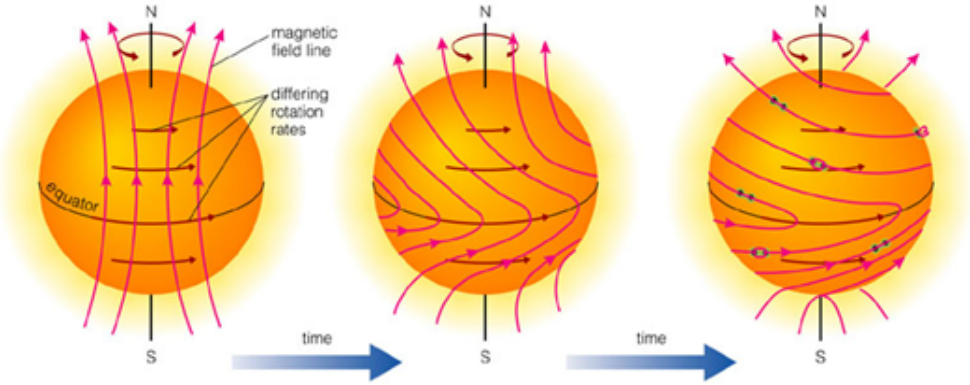

Figure 1.1: Differential rotation and its effects on the Sun's magnetic field (Bennett et al., 2012). Field lines are dragged across disk center, bending and twisting along the way.

On the surface the rotation rate is often referred to as synodic, meaning the time for a specific feature to rotate to the same apparent position, as viewed from Earth. The synodic equatorial rotation period is 26.24 days; however it is more common in astrophysical literature to use the Carrington rotation period of 27.2753 days. It corresponds to a rotation rate at 26 degrees latitude, a common

location for sunspot activity. Moreover, the polar rotation rate is around 35 days (Priest, 1995).

1.2.2 The Solar Cycle

Tracking the motion of sunspots and eruptive events has revealed the Sun's cyclic nature. The variation in sunspot number was first recorded by German astronomer Samuel Heinrich Schwabe (1843). His observations over a 17-year period revealed the 11-year cycle between maximum numbers of sunspots. It was later found that periods of maximum and minimum solar activity respectively correlate to higher and lower sunspot counts. Swiss astronomer Rudolf Wolf compiled these observations and others dating back to Galileo's first observations in the 1600's. Wolf even established a number scheme, counting the 1755 – 1766 cycle as number "1". Figure 1.2 illustrates the cyclic nature of sunspot variation.

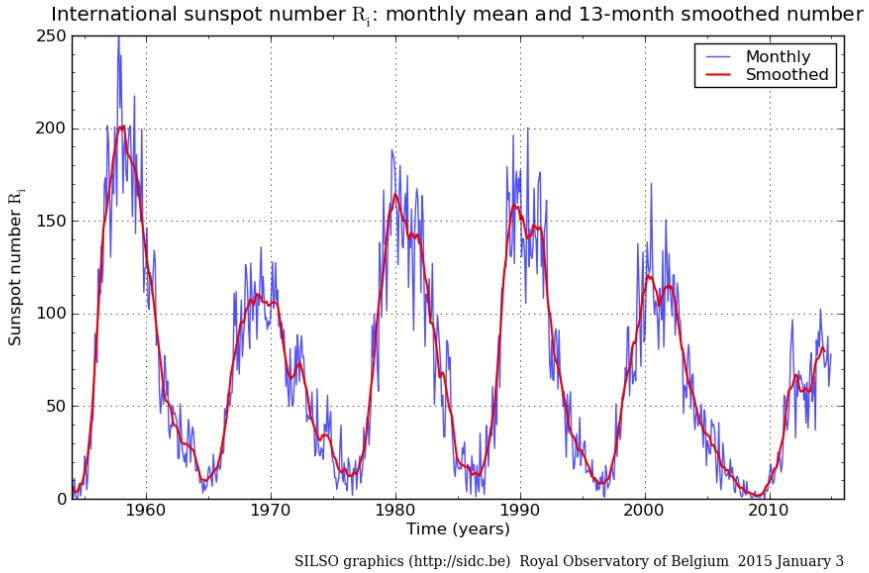

Figure 1.2: Sunspot number of 60 years, illustrating the 11-year solar cycle (SIDC, 2014).

It wasn't until 1908 that sunspots were determined to be paired magnetic regions of opposite polarity by George Ellery Hale. He also discovered that throughout the 11-year cycle, the polarity of sunspot pairs is normally the same in a given solar hemisphere, and opposite across hemispheres (Hale et al., 1919). For example, in one hemisphere all (or most) sunspot pairs have the positive polarity region leading with negative trailing, while the other hemisphere is the opposite. Hale's research revealed the Sun's true cycle, a magnetic cycle that reverses approximately every 22 years. It remains common practice to refer to the solar cycle in 11-year increments, although cycle lengths can vary between 9 and 14 years. The radial component of the Sun's magnetic field ($\mathbf{B}_r$) in solar latitude graphed against time displays the sunspot polarity reversals in a signature "butterfly" pattern, seen in Figure 1.3.

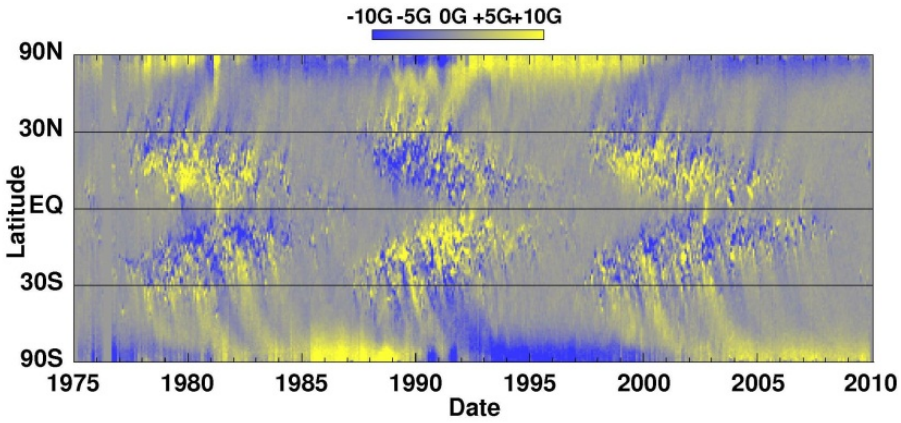

Figure 1.3: $\mathbf{B}_r$ (Gauss) over the solar surface against time, averaged over successive solar rotations (NASA MSFC, 2010). The infamous butterfly diagram shows the reversal of polarity ordering in hemispheres per solar cycle.

Currently, the Sun is entering into solar maximum during cycle 24. The predicted and observed sizes of sunspots make this the smallest sunspot cycle since Cycle 14. Solar maximum is marked by high sunspot numbers and an increase in magnetic active regions that are the source for solar eruptive phenomena. Total solar irradiance, or the amount of solar radiative energy incident on Earth's upper atmosphere, also increases during solar maximum.

1.2.3 The Solar Dynamo

It is well established in the solar physics community that the only conceivable way to generate the field strengths in the large-scale solar magnetic field is through a dynamo process. The idea of a hydromagnetic dynamo is based upon the concept that the motion of an electrically conducting fluid across a magnetic field will induce a current (Faraday's Law), which in turn will generate a magnetic field (Ampère's Law). Although the concept on a whole is widely accepted, exactly how it occurs is subject to much debate. It can be simplified to what is known as the kinematic problem. For example, the kinematic dynamo action is possible if a source for a velocity field can be found that is capable of regenerating both the toroidal and the poloidal components of the magnetic field (Bushby & Mason, 2004).

Helioseismic observations have well established that the ω-effect caused by the Sun's differential rotation (see Section 1.2.1) has its origins at the base of the convective zone (i.e., the tachocline). This provides a solution to half of the problem, where an initially poloidal field is stretched to have a toroidal component. The missing link to complete the dynamo cycle would have to explain how segments of toroidal loops can twisted such that they lie in the meridional plane. This is known as the alpha (α) effect. Over the past 60 years, there have been multiple explanations of how the α-effect could occur and where it could originate from (e.g., Parker, 1955; Babcock, 1961; Leighton, 1969).

Further, there is believed to be a highly localized second dynamo mechanism responsible for weaker perturbations in the solar surface magnetic field. It is very different in character compared to the large-scale dynamo and is thus treated separately (Cattaneo and Hughes 2001).

1.3 The Solar Atmosphere

The solar atmosphere resides immediately above the convection zone. This exterior region consists of three main layers, the photosphere, chromosphere, and corona, and extends out to the solar wind. The solar wind travels supersonically, filling a region defined as the heliosphere before slowing abruptly due to interactions with the interstellar medium. The heliosphere displays the reaches of the Sun's influence, believed to extend beyond the limits of the solar system.

Contrary to the dynamics of the interior, the structure and energy transport in the solar atmosphere is heavily influenced by the magnetic field. The ratio of gas pressure (p_{gas}) over magnetic field pressure (p_{mag}), defined to be the plasma β, determines whether the gas or the magnetic field will govern a given region. Plasma β is defined as:

$$\beta = \frac{nKT}{\frac{B^2}{2\mu_0}} = \frac{p_{gas}}{p_{mag}} \tag{1.1}$$

The magnetic field pressure is ${B^2}/{2\mu_0}$, where B is the magnetic field strength, and μ_0 is the permeability of free space. Within the interior, the gas pressure is much higher than the magnetic pressure, resulting in the energy generation and transport processes described in Section 1.1. Under these conditions $\beta \gg 1$ and the gas dominates over the magnetic field. However, plasma beta varies in the exterior layers of the Sun where β can be much less than one. Thus the magnetic field pressure dominates over the gas pressure, resulting in the magnetic field defining the structure and energy transport of the solar atmosphere (Kivelson, 1995).

1.3.1 The Photosphere

The photosphere, or the Sun's apparent surface, marks where the gaseous plasma is now visible in white light. Hot, high entropy gas is brought to the photosphere from convection cells, where excess energy is radiated away through this thin 500 km of stellar material. This region remains optically thin in visible, UV and near infrared continua. The photosphere is a cool 5800 K and a number of features are readily observable. The photosphere is typically studied at a variety of wavelengths in the visible including lines that exhibit Zeeman splitting, which can be used to measure the Sun's magnetic field. Magnetograms depict the spatial variations in strength of the solar magnetic field through exploiting the Zeeman effect, seen in Figure 1.4b. Near the solar surface, plasma β is typically around 1. However, in strong active regions β is much less than 1 and the magnetic field dominates, whereas in weak field regions the opposite holds true ($\beta \gg 1$) and the gas dominates over the field.

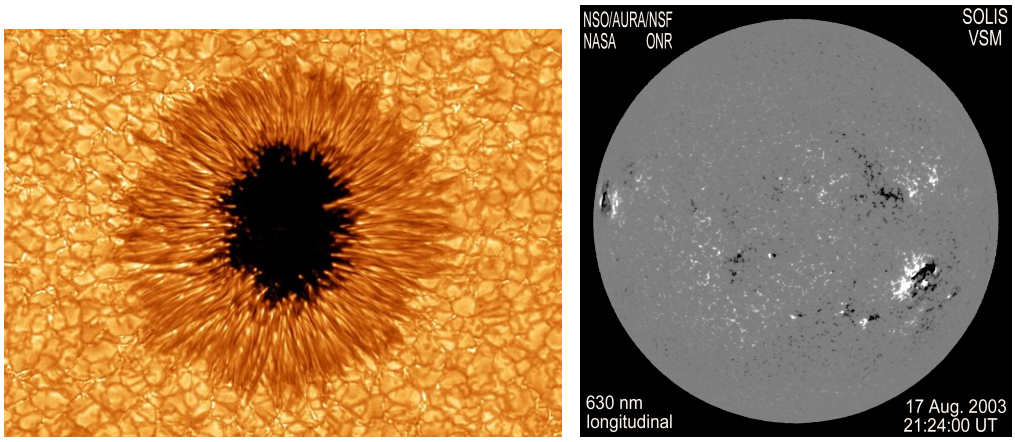

Figure 1.4: a) (left) High-resolution image taken with the New Solar Telescope (NST). This image highlights a sunspot and surrounding faculae forming the bright regions of solar granulation. **b) (right)** Magnetogram taken from Synoptic Optical Long-term Investigations of the Sun (SOLIS). Gray denotes the quiet Sun while the white and black represent paired regions of opposite polarity.

The sources of magnetic field phenomena in the solar atmosphere are often connected to active regions. Active regions are areas of concentrated, high magnetic flux with field strengths on the order of 1.2 kG. Sunspots are a primary manifestation of these regions within the photosphere, appearing as a dark blemish due to their average temperature being up to 2000 K less than the surrounding quiet Sun (Figure 1.4a). Sunspots are paired magnetic regions of opposite polarity with field strengths thousands of times stronger than Earth's magnetic field. Both active regions and sunspots represent signatures of closed flux regions, and can often be the same feature. Another feature that stems from active regions is faculae (Figure 1.4a), bright granular structures on the Sun's surface that are slightly hotter than the surrounding photosphere. Their fields are slightly weaker and more diffuse. Outside of active regions is the magnetic network comprised of significantly weaker (i.e., several Gauss) fields (Priest, 1995).

1.3.2 The Chromosphere

Above the photosphere, the solar atmosphere plasma continues to drop in density (to as low as 10^{17} m^{-3}) and temperature (to as low as 4,400 K) resulting in the interesting dynamics of the chromosphere. Plasma β now becomes less than one and the magnetic field begins to dominate. Unlike the photosphere, the chromosphere marks where temperature begins to increase travelling radially outward from the Sun. This reversal changes the primary observed spectra from absorption to emission lines. Notably unique layers of solar atmosphere can be defined through filtering out lines of weaker emission. The chromosphere, namely the "sphere of color", is best observable with a hydrogen alpha filter (656.2 nm) possessing a deep red hue. It is approximately 2000 km thick (Priest, 1995). Spacecraft and ground based measurements and imaging allow scientists to study the chromosphere. The Atmospheric Imaging Assembly (AIA) onboard

the Solar Dynamics Observatory (SDO) observes the chromosphere through the He II line emission at 50,000 K.

The features exclusive to the chromosphere are spicule and plages. Spicule are jets of dense gaseous plasma that move upward from the photosphere. Lasting for only about 15 minutes, they are often associated with high magnetic flux concentrations. Plages are believed to be connected with the faculae of the photosphere, due to their similar nature of being a bright region. Manifestations of active regions include prominences and filaments, which occur both in the chromosphere and the corona. They are the same feature but viewed from different perspectives. Prominences are massive, bright loops of plasma visible on the solar limb as extending out into the heliosphere for several Earth radii. Filaments are the same feature, but viewed against the disk center. The background sun makes filaments appear as dark crack-like features due to their lower temperatures against the background Sun (Priest, 1995).

Historically, there have been many theories to explain how the chromosphere is heated, beginning with Schwarzschild's theory (1948). He proposed that acoustic waves carrying kinetic energy from solar granulation could result in chromosphere heating. Today the two main branches of this debate are heating due to acoustic waves, and heating caused by magnetic reconnection (Sturrock, 1999).

1.3.3 The Corona

The outermost layer of the solar atmosphere, the corona, begins suddenly in a thin transition region with an extremely high temperature gradient. Plasma heats up from thousands to millions of Kelvin over only a few thousand km as seen in Figure 1.5. The exact mechanism of coronal heating is still subject to significant debate. The problem first became apparent when Grotrian (1939) and Edlén (1942) realized that emission lines seen during total solar eclipses were not

due to a new element dubbed "coronium," but rather to known elements at very high stages of ionization. There is consensus that there exist many different heating mechanisms involved in the corona. The dissension is centered around which heating process is dominant over small and large scales (Klimchuk, 2005).

Following suit with the Suns behavior in the chromosphere, the magnetic field pressure is much higher than the gas pressure. The gas density is 10^{-12} times lower that densities near the solar surface. Therefore, coronal structure is dominated by the evolution of the magnetic field beginning in the photosphere.

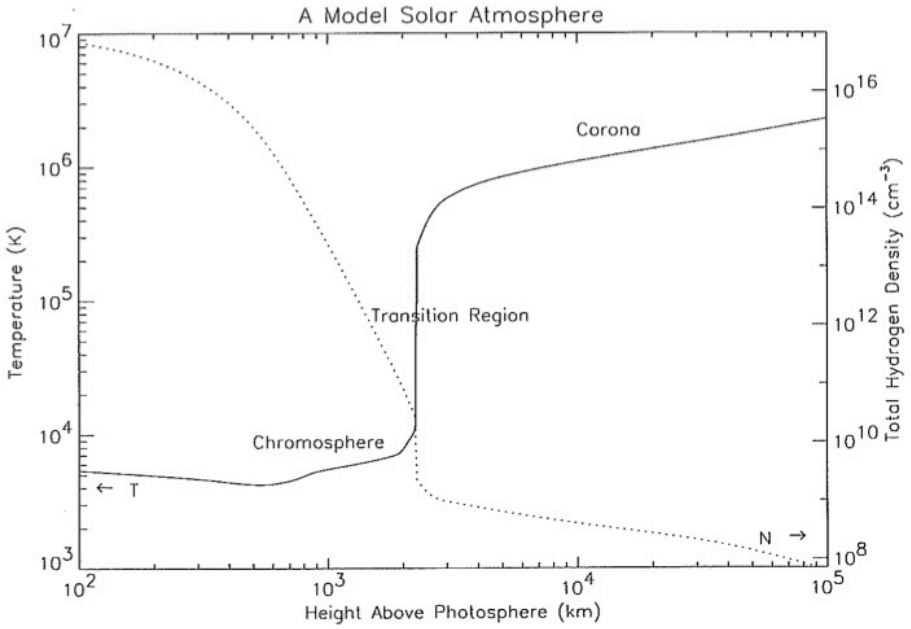

Figure 1.5: Temperature and Hydrogen density profile against height above photosphere (SAO, n.d.). The transition region is virtually a discontinuity by two orders of magnitude in temperature increase

The corona appropriately suits its translation from ancient Greek when viewed as a "garland wreath" during a total solar eclipse or through a coronagraph, shown in Figure 1.6a. It is much fainter than the photosphere and chromosphere because it is much less dense and most of the light is radiated in ultraviolet wavelengths. The light is mainly emitted at such short wavelengths due to high temperatures (millions of K). Having an intensity far lower than the

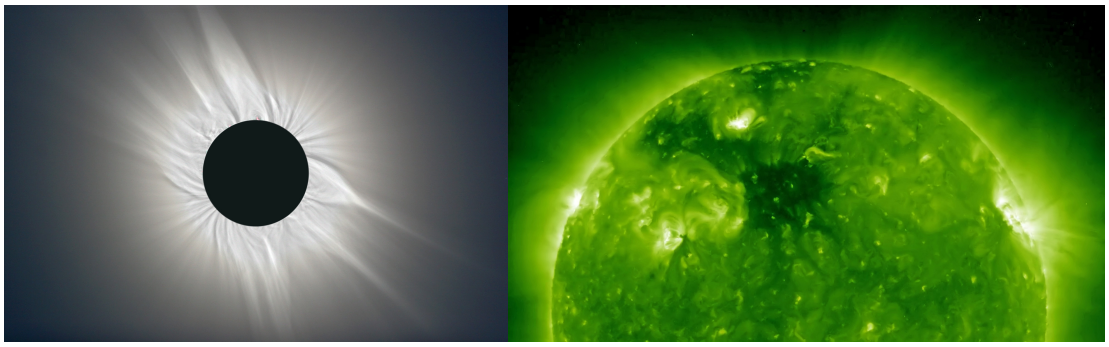

Figure 1.6 a) (left) White light coronal image. The radiation of the white light corona is due to scattering of photosphere photons by free electrons in the corona and interplanetary dust particles. The intensity of the white light corona is about 10^6 times smaller than the photospheric intensity. **b) (right)** EUV image of the corona. Bright loop signatures near the limb are prominences and coronal loops (closed flux sources), while dark regions on the disk are coronal holes (open flux sources).

photosphere, the corona must be imaged in specific wavelengths. Coronal structure is also revealed in white light eclipse of coronagraph images. This corona "emission" is actually photospheric white light scattered off electrons in the corona.

1.3.3.1 Closed vs. Open Magnetic Fields

As mentioned previously, the high temperature, low-density environment of the corona results in nearly fully ionized plasma with high conductivity causing the magnetic field to be fully coupled with the plasma motion. This is known as "frozen-in flux", where the magnetic field determines the plasma's framework and they move together as one. The Sun's differential rotation results in the deformity of field lines depicted in Figure 1.1. From this, two distinct components of the solar magnetic field are formed. The twisted field lines create magnetically closed loops extending the breadth of the solar atmosphere, with both footprints of opposite polarity grounded at the surface. These plasma-infused magnetic loops that are connected on both ends to the solar surface are

defined as "closed" magnetic fields. Observable phenomena in the lower corona that have closed field lines are coronal loops (filaments and prominences). In other cases, the magnetic field becomes so malformed that lines reconnect, releasing much of their stored energy in a sudden outburst. Large volumes of coronal material and embedded magnetic field are ejected out into the heliosphere during reconnection. These events are solar flares and CMEs, seen in the outermost layers of the corona. This type of activity is common during solar maximum.

When the field lines do not reconnect as during solar flares and CMEs, they can be dragged out into the heliosphere by the solar wind with one footprint still rooted at the solar surface. Essentially these field lines are concentrated unipolar flux tubes that extend out from the Sun and do not connect back within the solar atmosphere. They are defined as "open" magnetic field lines because they thread the heliopause before presumably reconnecting with the interstellar medium. In this way, open magnetic field lines do not violate Maxwell's Laws, which state that all magnetic fields must form closed loops (i.e., there are no magnetic monopoles). Coronal signatures that reflect open field regions are known as coronal holes. Not only are coronal holes magnetically open, they are typically cooler in contrast to the surrounding corona, rendering then visually dark in different wavelengths of images such as extreme ultraviolet (EUV). Solar minimum is marked by large coronal holes in the polar regions, while mid-latitude isolated coronal holes characterize solar maximum. Isolated coronal holes can have unipolar magnetic field strengths four times that of polar coronal holes during solar maximum (Arge et al., 2002). These features are illustrated in Figure 1.6b. Open magnetic flux is discussed in great detail in Chapter 2.

1.4 The Solar Wind

The corona, as seen in Figure 1.6a, is the region of the solar atmosphere with the lowest density and the highest temperatures. The gravitational and magnetic forces of the Sun are unable to contain the gaseous plasma heated to millions of Kelvin. The result is the outward flow of plasma supersonically away from the Sun, the solar wind. Solar material from below then streams up to replace lost matter expelling away at approximately 10^9 kg/s. First modeled by Eugene Parker (1958), the solar wind consists of a constant highly variable flow of charged particles filling and defining the limits of heliosphere.

Fast solar wind speeds travel at rates between 700 – 900 km/s and originate from the centers of coronal holes. Slow speed flows have a velocity between 300 – 500 km/s and can be three times as dense as the fast solar wind. The source of the slow solar wind is believed to be coronal boundaries, small coronal holes, active regions, and streamers that carry plasma along closed magnetic fields. Both the slow and fast solar wind send streams of ionized particles radially outward from the Sun. Adding in the effects of solar rotation, and the change in polarity among hemispheres, the solar wind forms an Archimedean spiral spanning the heliosphere (aka Parker Spiral). The boundary between polarities defines the heliospheric current sheet (Hundhausen, 1995).

The solar wind is the direct link between Earth and solar activity. Travel times for solar eruptive phenomena take about four days to breach Earth's magnetosphere. Large-scale events can cause geomagnetic disturbances that could damage important and costly space assets in the solar-terrestrial environment. Currently, the corona and solar wind are modeled in attempt to gain foreknowledge of solar activity that cause geomagnetic storms. An accurate report allows ample time to power down satellites in preparation for the oncoming overflow of charged particles.

1.5 Motivation

The Sun's magnetic field, first revealing itself in the photosphere, determines the structure and nature of the corona, and thus the solar wind and heliosphere. It is important to have a realistic understanding of the Sun's magnetic field to understand every layer of the Sun. The corona is arguably the most studied region of the Sun yet still begs much attention due to its complexity. Much of the explanation behind coronal heating remains ambiguous and more exhaustive definitions of coronal features are needed, all of which are connected to the Sun's magnetic field. Equally, there is a need to accurately understand the Sun's interaction with the solar terrestrial environment and its influence on Earth's magnetosphere. This relationship can be better understood through coronal and solar wind modeling, creating a strong motivation for model validation.

An indicator of how accurately coronal field models are representing reality is how well they represent the quantity of open magnetic flux. This is true because it is widely thought that coronal holes, a prominent feature of the Sun's corona, are the main source of open flux. An accurate determination of open flux is dependent upon a comprehensive definition of a coronal hole and correct boundary conditions to constrain those areas. Further, these regions are also the source of the fast solar wind. Introducing an alternative method to calculate open flux can reveal how well the models determine coronal holes, and thus the fast solar wind. It could also confirm sources of discrepancy between model and spacecraft data.

In the past open flux obtained from coronal field modeling has been compared against spacecraft observations in order to evaluate their accuracy. However, it is now well established that there are extended intervals over the solar cycle where significant discrepancies exist between the observed open magnetic flux based on spacecraft observations and that determined from coronal models, especially in the past decade (Owens et al., 2008; Lockwood et al., 2004,

etc.). This research proposes a different method using observationally derived coronal holes to calculate the open flux. The widely available global EUV imaging of the corona from spacecraft has made it possible to visually identify areas of open magnetic field. This approach provides a constraint to coronal hole areas that can be directly compared to model-derived values.

Analyzing different methods of determining open flux helps to determine what is causing the discrepancy between model predicted values and spacecraft data. The motivation for a new approach that manually derives coronal hole areas is to affirm one of two general scenarios: 1) the models are predicting open flux quite well and spacecraft data are suspect because they include sources of closed flux such as CMEs, especially near solar maximum, or 2) spacecraft data are more closely aligned with observationally derived open flux values, concluding that coronal models are missing key physics. Of course, specific sub-scenarios within each are also explored to pinpoint sources of uncertainty and work to rectify points in question.

Chapter 2: Methodology

2.1 Calculating Magnetic Flux

Total magnetic flux (Φ) is expressed as the surface integral of the normal component of the magnetic field ($\mathbf{B}$) passing through a particular surface:

$$\Phi = \iint_S \mathbf{B} \cdot d\mathbf{S} \tag{2.1}$$

If the surface is closed, Gauss's law of magnetism states that the total magnetic flux must be zero:

$$\Phi = \oiint_S \mathbf{B} \cdot d\mathbf{S} = 0 \tag{2.2}$$

This is a consequence of no magnetic monopoles ever being discovered, and can also be expressed as $\nabla \cdot \mathbf{B} = 0$. Ultimately, all magnetic field lines will eventually close (Griffiths, 2012).

On the Sun, the closed surface by which to calculate magnetic flux can be taken as a sphere at different heights above the photosphere. Nevertheless, an

enclosed spherical surface around the Sun would give a result of zero magnetic flux. Solar physicists like to distinguish between "open" and "closed" magnetic fields, where "open" refer to those magnetic fields that escape into interplanetary space, while "closed" magnetic field lines are ones with each end point rooted in the photosphere and never extending out into interplanetary space. In reality, there is no such thing as an open magnetic field. Those fields lines that do get carried away from the Sun by the solar wind always eventually connect with their oppositely directly magnetic field line counterparts in the outer heliosphere. To calculate either "open" or "closed" solar magnetic flux and obtain a nonzero value, the absolute value of the magnetic field's radial component ($|\mathbf{B}_r|$) must be used. The surface of integration is then the differential area of the sphere (dA) (see Figure 2.1).

In this work, the regions of open magnetic flux are desired. Using the technique described above, the nonzero open flux can be calculated through the summation of the absolute value of the field's radial component in the areas where the field lines are in fact "open". This is referred to as the unsigned open flux because the sign of $\mathbf{B}_r$ is removed for the summation. However, a fundamental issue is determining where solar magnetic fields are open and closed. Coronal models are often used to differentiate between these two regions because they provide a solution of the Sun's global magnetic field. In such models, each magnetic field line is traced to determine whether it is open (i.e., escapes into interplanetary space) or closed (i.e., starts and ends at the photosphere).

Alternatively, locations of open magnetic field can be determined by assuming that coronal holes are the main source of open flux, as discussed in Chapter 1. Knowing the locations of the Sun's coronal holes, as determined either by observations or a model, permits one to calculate the total (unsigned) solar open magnetic flux. Using observations is a new approach where coronal images in different wavelengths are used to determine where the coronal holes are located. In such cases, $|\mathbf{B}_r|$ is summed over each pixel of an image. Only the

pixels inside a coronal hole are kept in the summation, as per the following formula,

$$\Phi = \sum_{i,j}^{n} c_{i,j} \left|\mathbf{B}_{i,j}\right| r^2 sin\theta \Delta\theta \Delta\phi \tag{2.3}$$

where $\left|\mathbf{B}_{i,j}\right|$ is the radial field component at a given point on the surface (in this case, pixels of a global coronal image), $r^2 sin\theta \Delta\theta \Delta\phi$ is the differential surface area (dA) in spherical coordinates at that location, and $c_{i,j}$ equals one or zero, depending on whether the given point is inside or outside of a coronal hole.

Moving out into the heliosphere, beyond the point where all closed field lines have reconnected back to the solar atmosphere, all of the magnetic fields are open. One can then calculate total open flux simply by summing the (unsigned) magnetic flux over the entire surface. The magnetic global heliospheric field in this region can be, once again, derived using a model or using in situ spacecraft observations. In the latter case, a number of assumptions must be made about the nature of the global field must be made. The unsigned open solar flux typically varies by a factor of two over a solar cycle, peaking about a year or two after solar maximum (Arge et al., 2002).

2.2 Deducing Total Open Flux Using In Situ Measurements

Observations from the Ulysses spacecraft have shown that the term $R^2|\mathbf{B}_r|$ (where R is heliocentric distance and $\mathbf{B}_r$ represents the radial component of the Sun's magnetic field) is independent of latitude (Smith et al., 2001). While not anticipated, this result makes sense physically because as solar magnetic fields flow out into the heliosphere they come into magnetic pressure balance resulting in the global heliospheric field becoming on average very uniform. Thus, it follows that single point measurements of $\mathbf{B}_r$ made by a spacecraft located at

distance R from the Sun can be used to surmise the total (unsigned) open magnetic flux, $4\pi R^2|\mathbf{B}_r|$. Initially, Ulysses data showed that open flux values increases with radial distance, where it should remain constant (Arge et al., personal com., June 2014). This appears to result from a time variation of the magnetic field at large distances from the Sun. At such distances, the tangential component dominates the radial component in magnitude falling off as $1/r$ and $1/r^2$ respectively. On the contrary, at distances < 2.5 AU the radial and tangential components of the magnetic field are roughly equal in magnitude. Therefore, one can safely surmise the total open heliospheric flux using single point in situ measurements from space located at distances < 2.5 AU (Owens et al., 2008).

The data used to calculate the open heliospheric flux was the daily averaged radial component of the field ($\mathbf{B}_r$) from the low resolution OMNI (LRO) data set. All data are from spacecraft in L1 orbit from 1990 to 2013. From 1997 onward, the data are primarily from the Advanced Composition Explorer (ACE) spacecraft. From 1990 to 1997 the data are taken from of the International Sun/Earth Explorer 3 (ISEE-3), and the Global Geospace Science (GGS) Wind satellite launched in 1994. Both ISEE-3 and Wind are in halo orbits at L1. The OMNI data used were the daily averaged radial component of the magnetic field in the Geocentric Solar Ecliptic (GSE) coordinate system, corresponding to $\mathbf{B}_x$. The x-axis in the GSE coordinate system points from the Earth towards the Sun. Using data from L1 orbits ensures that the values of $\mathbf{B}_r$ will not be affected by the magnetosphere. Also, by using the daily averages of $\mathbf{B}_r$, rapid fluctuations from Alfvén waves should be averaged out because these fluctuations occur on much smaller timescales. For this research, the magnitude of each daily averaged $\mathbf{B}_r$ value is taken and then plotted over a 3 Carrington rotation average. Thus, the results in this research are presented as averages over approximately 81 days of the magnitude of $\mathbf{B}_r$.

There are some notable pitfalls to spacecraft observed open flux. One of these are fluctuations in the tangential component may produce erroneous radial

fields as observed by spacecraft at large distances from the Sun (i.e., past Mars, >2.5 AU). Another is that spacecraft data may at times include sources of closed flux, such as CMEs that have propagated out and whose footprints have yet to detach. This is especially true during solar maximum when CMEs are more frequent. This is explored and discussed in depth in Chapter 4.

2.3 Potential Field vs. Magnetohydrodynamic Modeling to Determine Open Flux

Open flux can be derived using what is known as the Potential Field Source Surface (PFSS) model (Schatten et al., 1969; Altschuler & Newkirk, 1969; Wang & Sheeley, 1992). PFSS models essentially extrapolate the photospheric magnetic field out to a height known as the source surface. The model assumes that there are no significant electric currents, including displacement currents in the corona. Therefore Amperes law reduces to:

$$\nabla \times \mathbf{B} = 0 \tag{2.4}$$

The field can now be represented as a scalar potential Ψ, allowing the corona to relax to a minimum energy:

$$\mathbf{B} = -\nabla\Psi \tag{2.5}$$

Applying the divergence free condition:

$$\nabla \cdot \mathbf{B} = 0, \tag{2.6}$$

the above equations reduce to the Laplace boundary problem for the volume of the corona, which can be solved using separation of variables:

$$\nabla^2\Psi = 0 \tag{2.7}$$

In spherical coordinates, the general analytic solution is an expansion of spherical harmonics (Schatten et al., 1969; Altschuler & Newkirk 1969). The lower boundary is taken to be the observed photosphere magnetic field. An outer boundary can be introduced, the source surface, which forces all field lines that reach this surface to be radial (Figure 2.1). The radius of the outer source surface is a free parameter; however, it is typically chosen to be 2.5 $R_\odot$ to compute the optimal open flux compared to in situ data measurements (Hoeksema et al., 1983).

Wang and Sheeley (1992) argued that inferred radial component after line-of-sight projection correction should be used for the photosphere magnetic field (lower boundary):

$$\nabla\Psi \cdot \hat{r}\Big|_{r = R_\odot} = -\mathbf{B}_r\Big|_{r = R_\odot} \tag{2.8}$$

$$\nabla\Psi \times \hat{r}\Big|_{r = R_\odot} = 0 \tag{2.9}$$

where $\hat{r}$ is the unit radial vector and $\mathbf{B}_r$ is the radial field. Again, the outer boundary is essentially an artificial construct that forces a point that beyond which everything is open, where the field is required to be radial as seen in Figure 2.1.

The PFSS model can reproduce the large-scale magnetic field of the corona quite well, even when compared to more complex models incorporating magnetohydrodynamics (MHD). MHD solutions provided a more advanced description of the Sun's corona however they can give results similar to that provided by potential field models (Riley et al., 2006, de Toma et al., 2005). The PFSS model has the advantage of being far more computationally efficient and simple to implement compared to MHD driven models. Therefore PFSS models

provide a simple, straightforward method for determining open flux. Drawbacks associated with PFSS modeling are its inability to provide insight on certain plasma and thermodynamic properties of the corona, as well as not being able to determine the magnetic field beyond the chosen source surface height.

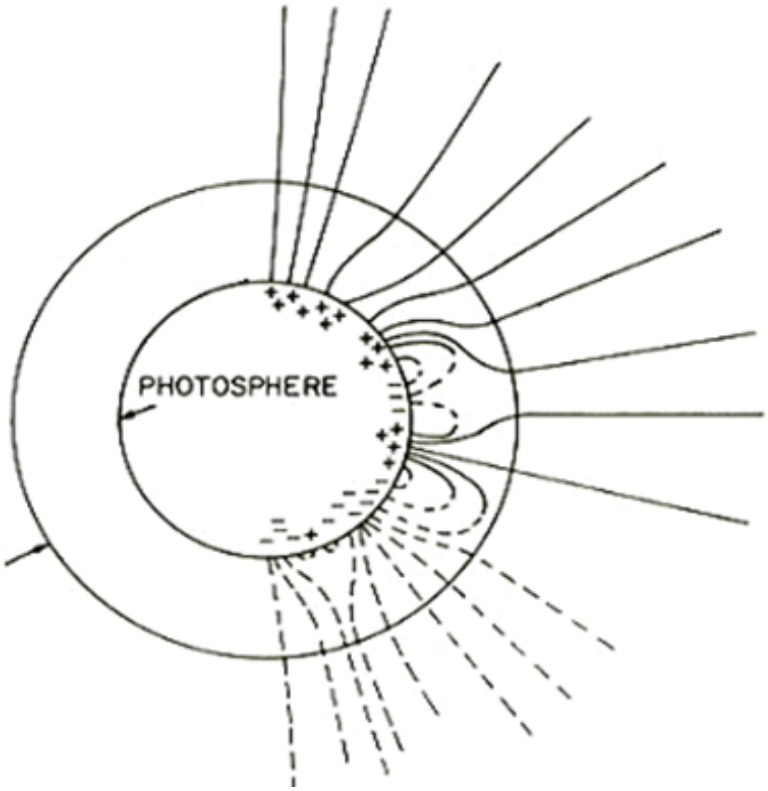

Figure 2.1: Magnetic field depicted at source surface height (Schatten, 1971). At heights extending into the heliosphere, the magnetic field becomes extremely uniform and radial. This makes it possible to enforce an artificial construct to surmise the total open flux. The source surface height is typically taken to be 2.5 $\mathbf{R}_{\odot}$.

2.3.1 The Wang Sheeley Arge Model

PFSS models and their resulting coronal magnetic structure can be combined with other models to further model the corona and predict the solar wind. The Wang-Sheeley-Arge (WSA) model (Arge & Pizzo, 2000, 2003b, &

2004) is one such model that is both empirical and physics based. It is driven by global images of the observed photosphere magnetic field in the form of a synoptic map. These maps are a model within themselves, as they can be derived from observation in many different ways. The various types of input maps are discussed further in Section 3.1. WSA first re-grids the input synoptic map (generally in longitude, sine-latitude coordinates) to a uniform resolution (i.e., grid cells in units of square degrees) specified by the user. The total magnetic flux is calculated over the map and any residual monopole moment is uniformly subtracted from it to ensure that the magnetic field is divergence free.

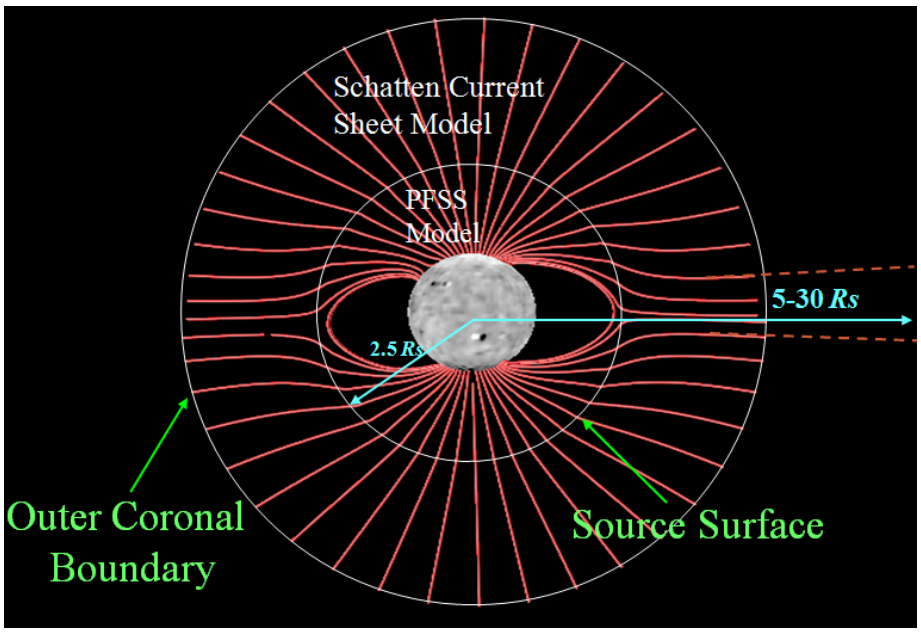

Figure 2.2: Coupled PFSS and SCS model (Arge, n.d.). The red lines are the coronal magnetic field lines as predicted by the model. This diagram displays the solution range most often used, from 2.5 $\mathbf{R}_\odot$ to anywhere between 5 and 30 $\mathbf{R}_\odot$.

The corrected map is then used in a magnetostatic PFSS model that determines the coronal field out to 2.5 $R_\odot$. The output of the PFSS model serves as input to the Schatten Current Sheet (SCS) model (Schatten, 1971), which provides a more realistic magnetic field topology of the upper corona. The SCS solution represented in Figure 2.2 extends radially out to infinity, however only a range of

the solution is used from the source surface height (typically 2.5 $R_\odot$) to the outer coronal boundary (set by the user normally between 5 and 30 $R_\odot$). The modeled coronal field provides locations of coronal holes through the tracing of field lines back to the photosphere as seen in Figure 2.3c. Essentially, the model tells the user where the regions of open flux are, and what the flux is for the given magnetic field input. Additionally, the model gives the solar wind speed at the outer coronal boundary surface using an empirical velocity relationship (Arge et al., 2003b & 2004), as seen in Figure 2.3a and b. The solutions from this figure can be fed into an advanced 3D MHD model of solar wind propagation. Densities and temperatures, which are not provided by WSA, may be deduced by assuming mass flux conservation and pressure balance. When WSA is used to drive an MHD solar wind model, the outer coronal boundary is typically set to a value beyond 15 $R_\odot$ to ensure that the solar wind is supersonic and super-Alfvénic.

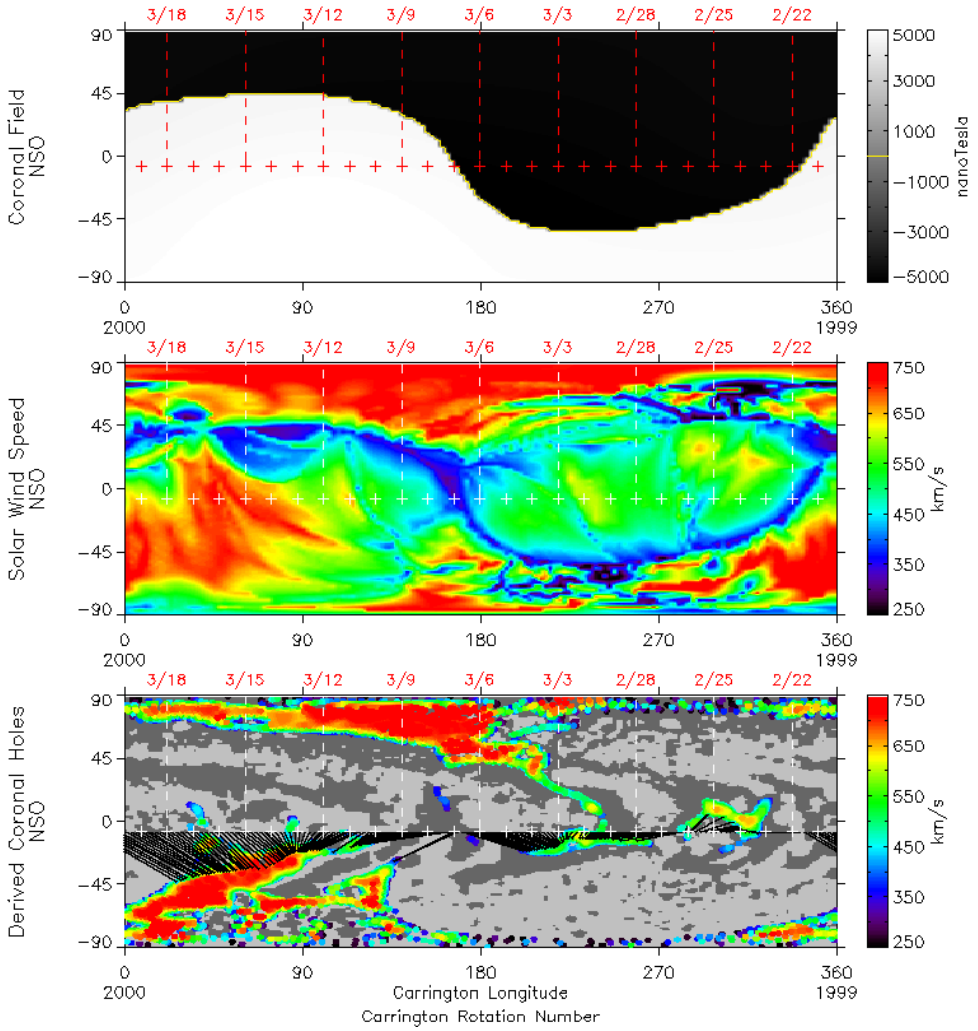

Figure 2.3: a) (top) Global coronal field polarity at 5 $R_\odot$. White areas indicate outward magnetic field while black illustrates inward magnetic field. The red (or white in the middle and bottom plots) plus signs near the equator mark the daily positions of the sub-earth point, indicating central meridian longitude of the Sun over time. **b) (middle)** Solar wind speed at 5 $R_\odot$ as predict by the model. **c) (bottom)** Coronal holes as determined by the WSA model. The field polarity at the photosphere is indicated by the light/dark (positive/negative) gray contours, while the colored regions reveal the foot points of the open field lines at the photosphere. The dot color indicates the solar wind speed at 5.0 $R_\odot$ as predicted by the model. The black straight lines identify the connectivity between the outer (open) boundary located at 5.0 $R_\odot$ and the source regions of the solar wind at the photosphere (1.0 $R_\odot$).

2.4 Historical Results

There is a wealth of prior work on the subject of comparing derived open flux from models and spacecraft data (Owens et al., 2008; Riley et al. 2006; Lockwood et al., 2004, etc.). Historically, the two seem to agree quite well on average seen in Figure 2.4. However, there are periods over which there is almost an anti correlation (1984 – 1988), and the two begin to deviate in 1999. Figure

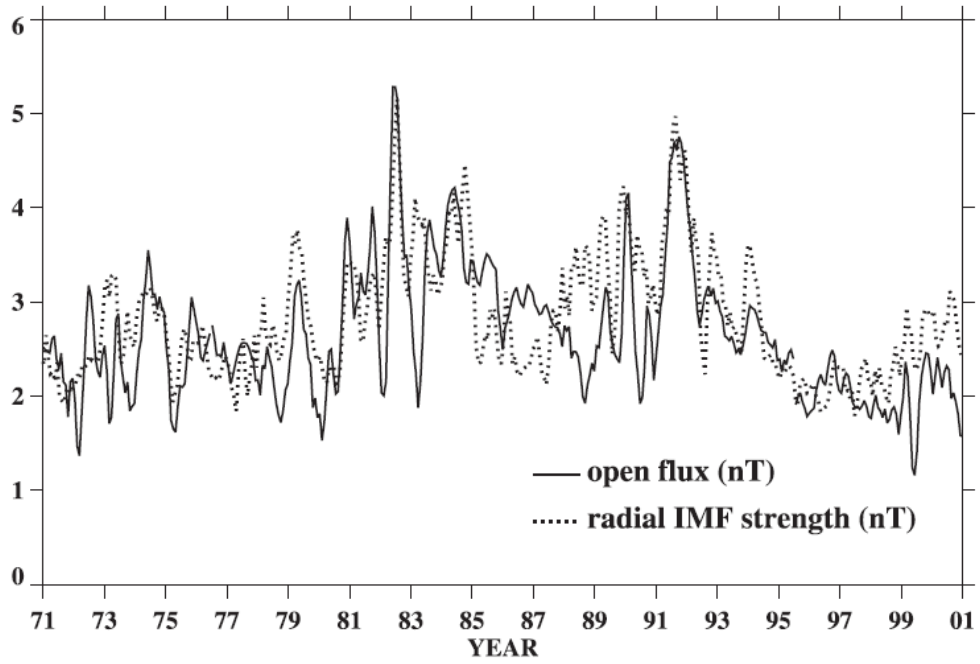

Figure 2.4: Spacecraft observation radial field strength and model-derived open flux from 1971 to 2001 (Wang, Sheeley 2002).

2.5 shows an extension of this data to the year 2013. The in situ results are depicted in red, and the WSA model-derived open flux is shown in dark blue. The two best coincide near solar minimum (1994 to 1998) indicated by the vertical dashed line during this time period. The second vertical dashed line (left to right) marks solar maximum, and the third denotes the most recent solar minimum.

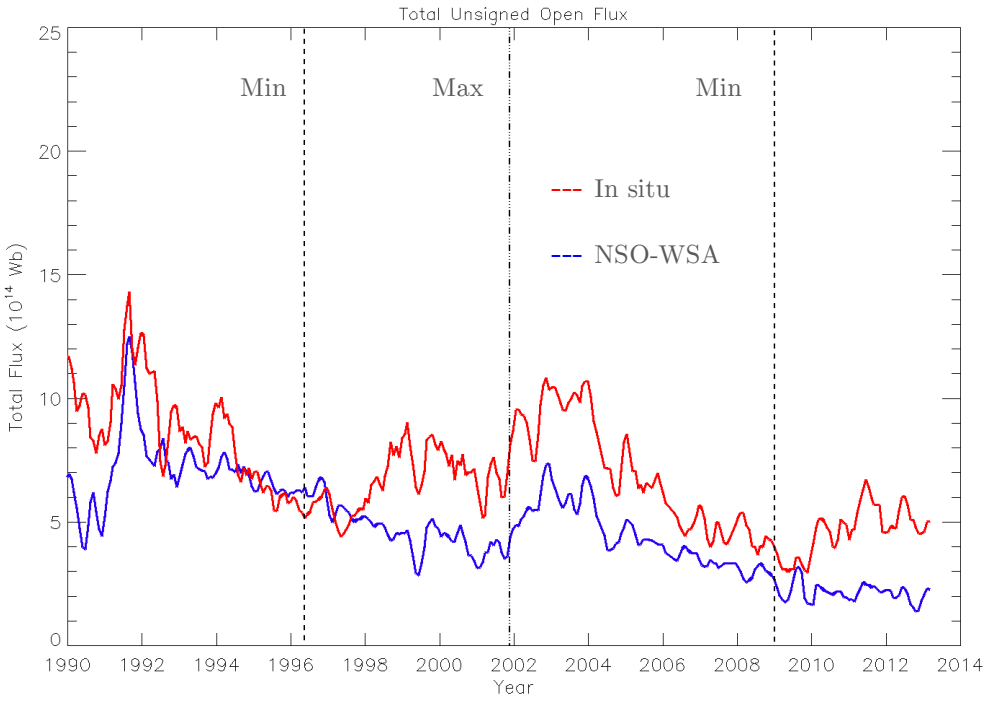

Figure 2.5: Comparing model-derived (blue) and spacecraft observed (red) total unsigned open flux (10^{14} Webers) from 1990 to 2013. The OMNI data set is the source for the heliospheric observations and the model data set is comprised using NSO KPVT and VSM inputs maps of the solar magnetic field into WSA. All data shown is plotted as a 3 Carrington rotation running averages. Black dashed lines beginning with solar minimum in 1996 mark periods (left to right) of alternating extremes in solar activity.

Starting in 1998 there appears to be a persistent offset between the spacecraft observed and model predicted open flux data sets, with the most significant discrepancies near solar maximum. This result is presently well established, giving rise to the motivation for this research.

Chapter 3: Alternative Methods

The use of in situ measurements and models are among the most common methods for determining open flux. The objective of this research is to use alternative methods for estimating total open heliospheric flux in order to investigate the potential sources of discrepancies between the values obtained through traditional means. Alternative approaches can shed light on how the magnetic field input affects potential field models and how well models determine coronal hole locations and areas.

3.1 Varying the magnetic field input

3.1.1 Traditional Approach (Diachronic Maps)

Potential field models as discussed in Section 2.3.1 require an input: the observed photospheric field. Conventionally, these global maps are made from observations of the Sun's magnetic field accumulated over a synodic 27.2753-day solar rotation, without accounting for known magnetic field transport processes such as differential rotation, supergranulation flows, meridional drifts, etc.

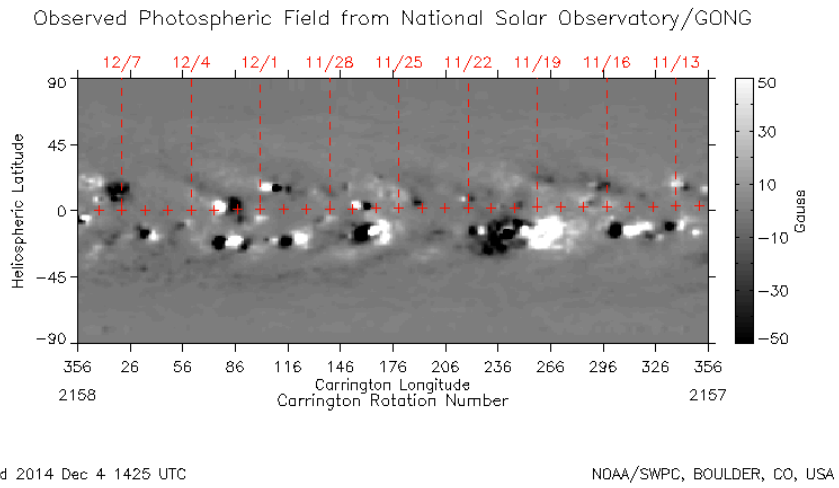

Figure 3.1: Synoptic map of the observed photospheric field for Carrington rotation 2158 (NOAA/SWPC). Each day over the whole rotation, the magnetogram disk image is remapped and added sequentially, forming a time history map of the central meridian. The longitudes of the central meridian, or sub-earth points, are denoted in red. The most recent data is on the left.

They are prepared in a variety of ways, such as slicing a thin area at the central meridian from a daily line-of-sight magnetogram in the rotation period. These slices are then remapped sequentially into heliographic coordinates (Figure 3.1) and assume that the magnetic field is radial. This technique also assumes the large-scale field does not change drastically over one solar rotation. Further, solar magnetic field data at any moment in time are only available for about half of the solar surface. Due to the lack of far side observations, over one solar rotation a synoptic map contains data at least 13 days old (Arge et al., 2010).

Traditional synoptic maps of the photospheric field represent a time history of central meridian evolution, thus *diachronic* by nature. The term "synoptic" is a misnomer because these maps do not represent the field at one given moment in time (Linker et al., 2013). These static maps of the global field mix space and time and do not allow for an accurate representation of magnetic signatures (Arge et al., 2010). Nevertheless, diachronic maps have been the convention used by solar scientists to represent the Sun's global magnetic field distribution.

3.1.2 Using Synchronic Maps

Diachronic maps of the Sun's magnetic field do not capture the Sun's evolution and time-dependent behavior. Therefore, there is a strong motivation to use a global map of the photosphere that represents the magnetic field at one given point in time. The Air Force Data Assimilative Photospheric Flux Transport (ADAPT) Model (Arge et al., 2009, 2010, & 2013) provides a *synchronic* (instantaneous) representation of the global field by evolving the flux using well-understood flux transport processes where observations are not readily available. The magnetic flux transport model used with ADAPT is a modified version of the Worden and Harvey (WH) model (2000). In addition to accounting for differential rotation, this model accounts for meridional flow that transports flux from the equatorial region to the poles. It also statistically accounts for solar activity that cannot be represented entirely through observation, such as the supergranulation that diffuses the magnetic field and random flux emergences. ADAPT is an ensemble model, producing 12 possible realizations of the global magnetic field to provide the best estimate of solar flux distribution at any given moment in time.

Flux transport models and traditional Carrington maps assimilate new data by simply inserting or blending directly with the evolving model. These blending methods make simplifying assumptions about the accuracy of the data and model. The ADAPT model incorporates various assimilation methods within the Los Alamos National Laboratory (LANL) data assimilation framework. ADAPT has the option to use either an ensemble least squares (EnLS) estimation (Bouttier & Courtier 2002) or Kalman filter (Evensen 2003) technique. The method that is currently used most often, and the one used to make the maps for this research, is the EnLS estimation. It takes into account errors both in the model and in the data, but does not consider spatial correlations whereas the Kalman filter technique considers past spatial and

temporal correlations between different regions of the photosphere (Arge et al., 2010).

Using the least squares or ensemble Kalman filter methodology allows new data to be assimilated with the evolving model to provide the best estimate of the global field. This process accounts for both the uncertainties of the model and the available data. For example, the ADAPT maps are heavily biased to observations near disk center because the magnetic field observations are very reliable with low uncertainty. However, polar region observations of the solar magnetic field are much less reliable, making these regions derived primarily by the model.

The goal of ADAPT is to provide the best estimate of the global spatial variation of the solar magnetic field for any given moment in time. The ADAPT model is a powerful tool used to synchronically represent the global field, a more realistic alternative to the traditional approach. These maps can be used as input into potential field models to derive the coronal field. Varying the input magnetic field into WSA using synchronic and diachronic maps allow for a unique comparison to see how the model derives the coronal holes for each, and thus the open flux. Further, both synchronic and diachronic maps of the Sun's magnetic field can also be used with coronal hole observations to physically derive open magnetic flux. These results can be compared with model and in situ values to help understand sources of disagreement between the various approaches.

3.2 Observationally Derived Coronal Hole Map Overlays

To compare with model predicted values of open flux, an alternative technique was implemented using observationally derived coronal holes to calculate the total open flux in open field regions. This method involved manually contouring coronal holes using global maps of the Sun's corona

assembled from EUV and Helium disk images. Once determined, the contoured coronal hole regions were overlaid onto the same magnetic field maps used as inputs into WSA to calculate open flux. In this way, the open flux is calculated by summing over each of the field regions inside a coronal hole boundary (see Section 2.1).

3.2.1 Helium data

Observationally derived coronal holes have been used in the past to study their evolution, as well as coronal magnetic activity. Karen Harvey and Frank Recely manually derived coronal holes from He I 1083 nm spectroheliograms to study the evolution of polar coronal holes during solar cycles 22 and 23 (2002). In addition, their coronal hole contours were overlaid onto NSO KPVT maps of the photospheric magnetic field to calculate the unsigned open flux. Both the spectroheliograms and the magnetic field maps are diachronic by nature.

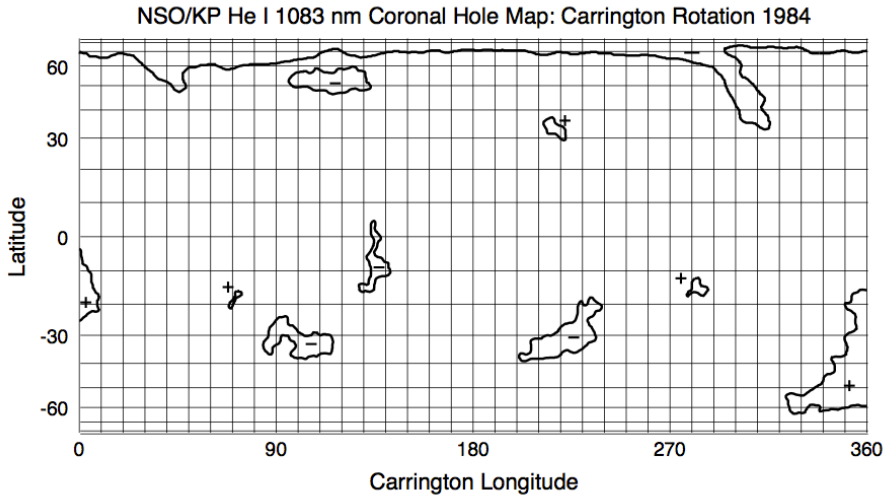

Figure 3.2: Coronal hole maps created from He I 1083 nm spectroheliograms (Harvey and Recely, 2002). Each map represents the coronal hole locations over an approximate 27-day Carrington rotation, verses a more realistic "snapshot" representation of the Sun at any given moment in time.

Together they make an accurate pairing to calculate the open flux because they are both represent the Sun as a time history of the central meridian over one Carrington rotation. Although, as discussed in Section 3.1.1, diachronic maps have significant drawbacks. An example of Harvey and Recely's coronal hole maps is shown in Figure 3.2. This data set begins in 1989 and ends in 2002. The open flux derived using He 1083 nm coronal holes and diachronic photospheric field maps (Harvey and Recely's original calculations) were used as a data set in this research. Additionally, the He derived coronal holes were converted to a Flexible Image Transport System (FITS) file. This allowed for the synchronic ADAPT maps to be more easily used with the He coronal holes to calculate the open flux.

3.2.2 EUV data

With the advent of recent spacecraft missions, the corona can now be represented globally in EUV. One such mission, NASAs Solar Terrestrial Relations Observatory (STEREO) mission, launched in 2006 consists of two satellites in a heliocentric orbit, one ahead (A) and one behind (B). In February 2011, STEREO A and B were 180 degrees apart, capturing the first ever 360-degree image of the solar corona. The Sun Earth Connection Coronal and Heliospheric Investigation (SECCHI) instrumentation suite captured these images with its Extreme Ultraviolet Imager (EUVI) with four different band pass filters. With these images and applying the same technique used by Harvey and Recely, the equivalent of coronal synchronic maps were created. During periods where the two satellites STEREO A (ahead) and B (behind) are separated such that they cannot capture the global solar corona, EUV images from the Atmospheric Imaging Assembly (AIA) were used to fill in the data gap. The AIA instrumentation suite onboard the Solar Dynamics Observatory (SDO) consists of four telescopes that image the Sun in a variety of EUV, UV, and visible-light

wavelength bands. Seven different EUV channels image the corona through different spectral patterns of highly ionized iron and He II. Each of these species occurs at different temperatures (600,000 to 10 million K) correlated to a height above the photosphere. The closest match to make synchronic global maps of the corona was to use STEREO data from the Fe XII 195 Å and AIA 193 Å Fe XII line emission (Pattichis et al, 2014). An example of these maps can be seen in Figure 3.3.

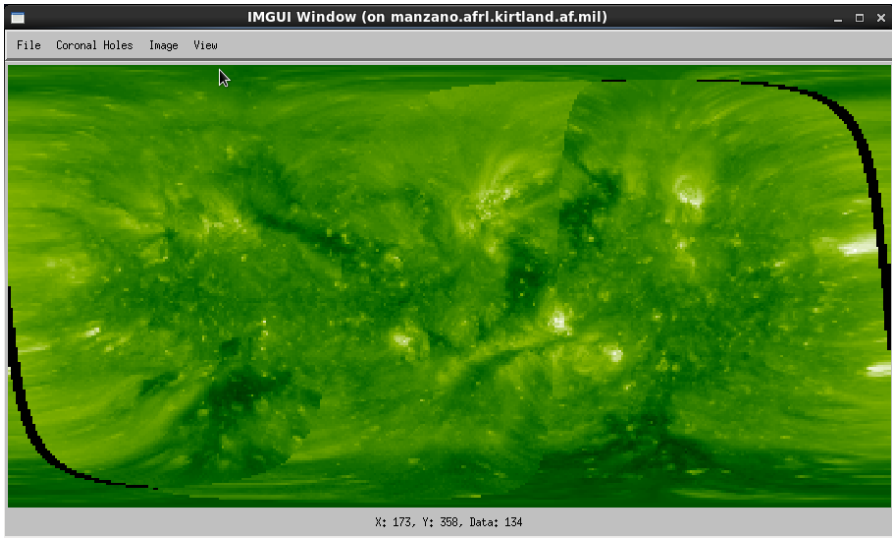

Figure 3.3: Synchronic EUV map of the corona. Maps were created using STEREO B (left), AIA (middle), and STEREO A (right).

The available images allowed for maps to be created spanning the years 2007 to 2013, representing Carrington rotation 2056 to 2135. Maps corresponding to the first and mid rotation date of each Carrington rotation were chosen to be included in this data set. Global EUV maps present a nice opportunity to pair with ADAPT maps of the Suns magnetic field when calculating the open flux, since they are both synchronic representations the Sun. Coronal holes were manually identified on each map using strict criteria (Figure 3.4). From Section 1.3.3, coronal holes are magnetically open regions of

lower density and temperature compared to the background corona, rendering them visually dark in EUV. These characteristics allow the coronal holes to be contoured separate from the background corona. An IDL routine (Pattichis et al., 2014) was used to display each remapped global EUV image. Locations of coronal holes were determined first by inspecting these images for concentrated areas of darkness. Contours were then overlaid onto the image to reveal the magnetic neutral lines (explained in Figure 3.5). This feature of the routine provided confirmation of regions with magnetically open fields, and helped rule out filament structures (closed magnetic fields).

Once a feature was determined to be a coronal hole, the full disk images from STEREO and AIA were used to reveal the areas true shape and coverage. If an area in question was in the middle portion of the global EUV map, it could be checked against the AIA 3-color channel image for that particular day (Figure 3.5). Coronal holes in this image appear deep blue, verses filaments that have a reddish hue. Once confirmed, coronal holes were contoured (Figure 3.6a) manually inside the IDL routine. The routine features a zoom tool for detailed contours to be made. The program outputs a binary mask FITS file (Figure 3.6b), known as the "ground truth" file that is used to represent which pixels are inside a coronal hole. The mask files were used with synchronic ADAPT maps to sum the individually calculated open flux for each pixel, over the entire solar surface (see Section 2.1).

Manually derived coronal holes are a necessary yet time consuming component of this research. Having a manual database of contoured coronal holes provides a standard that can be used to validate model-derived coronal hole locations and areas.

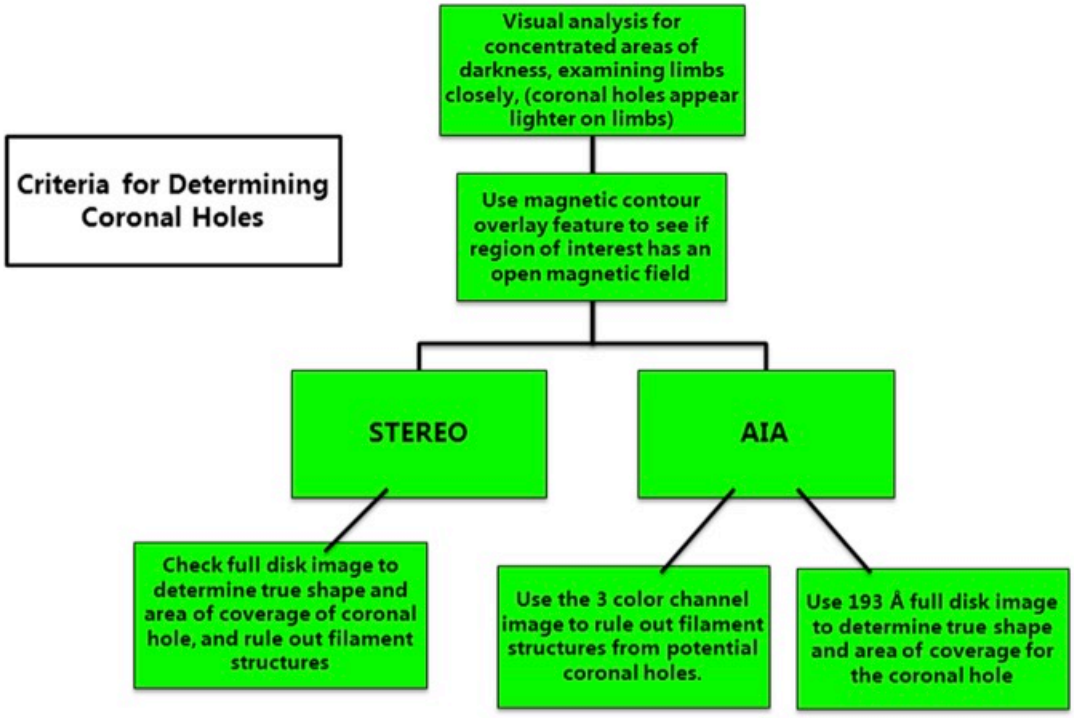

Figure 3.4: Criteria for contouring coronal holes in EUV.

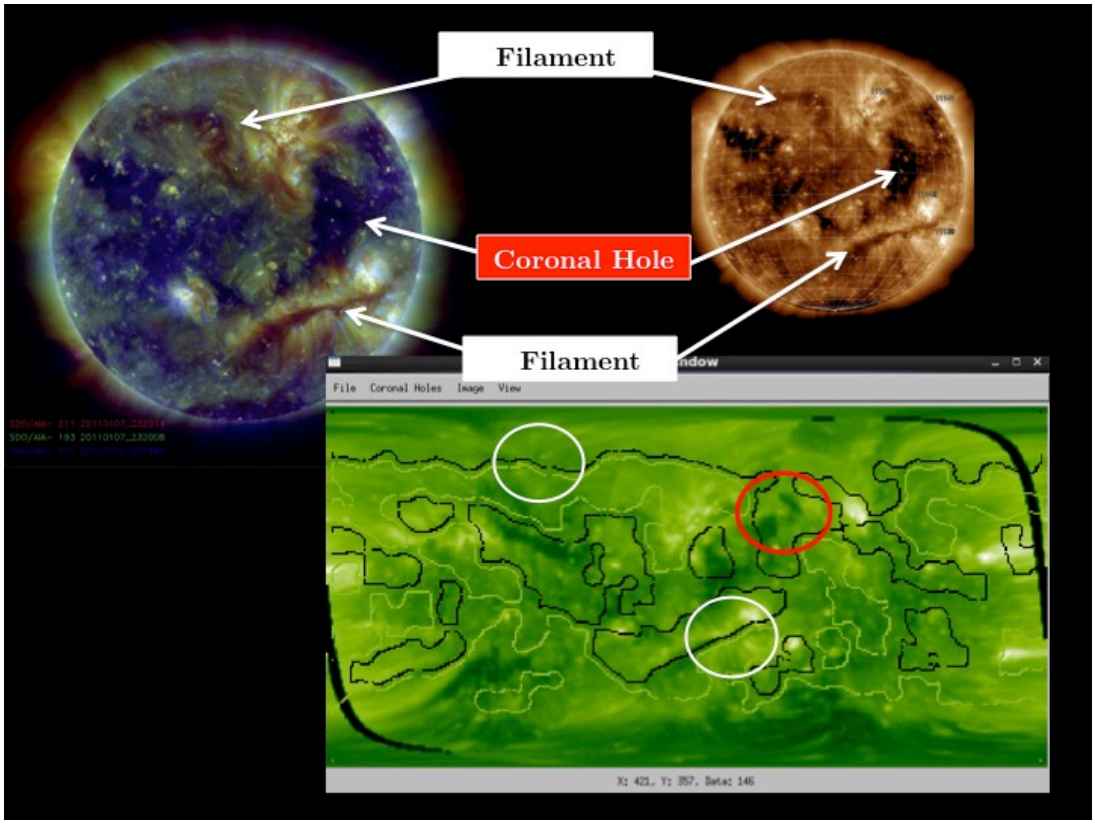

Figure 3.5: Differentiating between coronal holes and filaments using full disk AIA 3 color channel image (top left) of the Sun (SDO LMSAL, 2011). Filaments in this type of image have a distinct red hue, compared to the deep blue of the coronal holes. These specific filaments (white circle) and coronal hole (red circle) can be seen in the EUV global map of the corona for this same day (bottom). The EUV map is shown with the magnetic contour overlay feature. Filaments structures have two lines running close together separating regions of opposite polarity, whereas coronal holes are enclosed by a magnetic contour revealing a region of unipolar field. The true shape of a coronal hole can be verified using the AIA 193 Å full disk image (top right). The images shown are for January 6th, 2011.

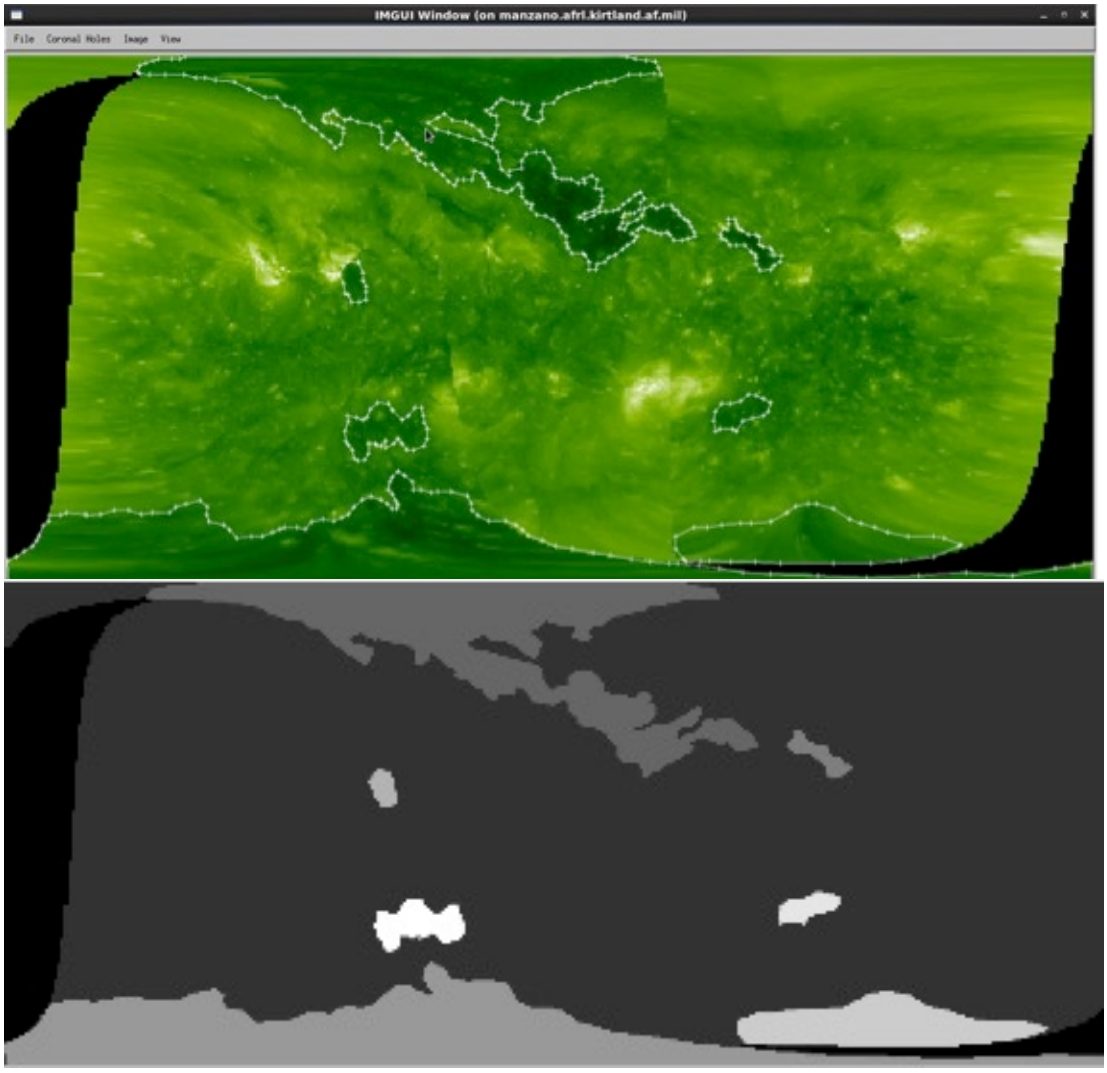

Figure 3.6: a) (top) Contoured coronal holes on a global EUV map for July 27th, 2010, the mid-rotation date of CR 2099. **b) (bottom)** Mask image of coronal hole areas and boundaries. The mask is a binary file that stores a '1' for every pixel inside a coronal hole boundary. These output files were used to overlay onto synchronic ADAPT maps to calculate the open flux, similar to that of Harvey and Recely's work.

3.2.2.1 Splicing EUV Images to Calculate Open Flux

Figure 3.6a brings to light one of the setbacks in using EUV data to create global maps of the Sun. For this particular day, and a majority of the others, data are missing on either side of the STEREO images. This is simply due to the separation between the two satellites not being 180 degrees apart at all times. Thus, calculating the open magnetic flux directly from one global EUV map would not accurately represent true solar conditions due to missing regions.

In order to correct for this problem, each of the coronal hole mask images were cut and stitched together with the preceding and succeeding maps. As mentioned in 3.2.2, the first (0 degree), middle (180 degree), and last (360 degree, i.e., the first day of the next CR) days of each Carrington rotation in the dataset were used to identify coronal holes. Each image was then cut into 90-degree segments. The open flux for an image was calculated by overlaying the observed coronal holes onto the corresponding ADAPT map for that date. Therefore, for each day the open flux was calculated in four 90-degree segments. The middle 180 degrees (2^{nd} and 3^{rd} slices of each image) all contained enough data, however the first and last 90-degree segments were incomplete. In order to correct for this problem, data from the first, middle, and last days of each rotation were used to build a map to represent the Carrington rotation as depicted in Figure 3.7. This allowed for the open flux to be calculated without any missing data.

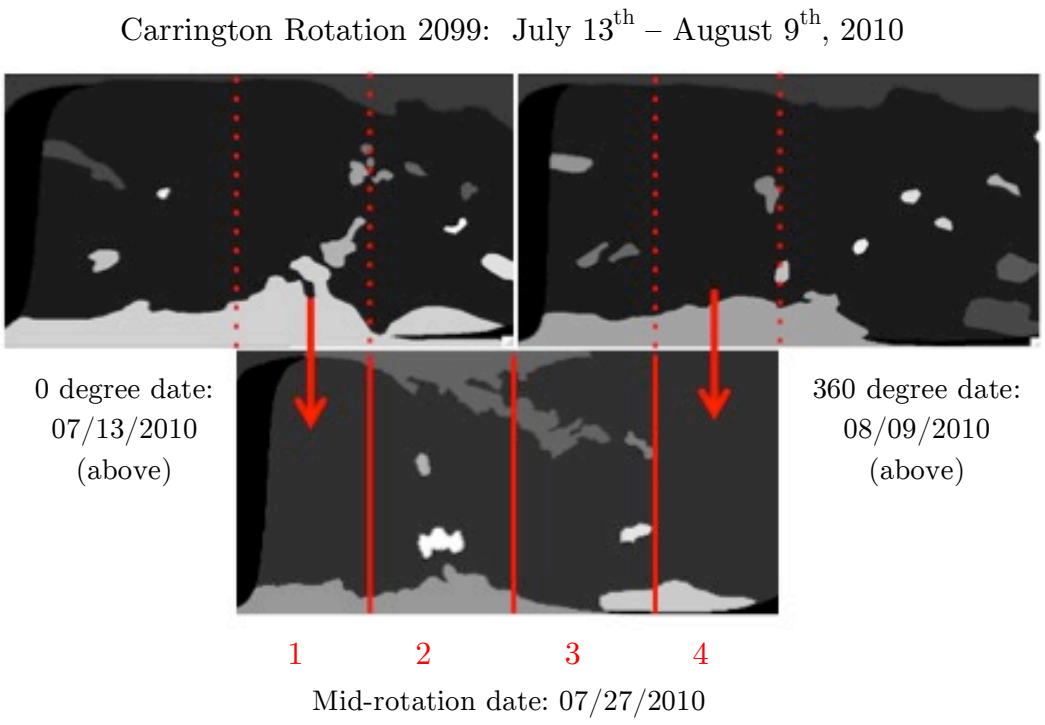

Figure 3.7: Cutting and stitching of mask images made from EUV derived coronal holes. The example above is for Carrington rotation 2099. The date marking the middle of this rotation is the map being created. To remove periods of missing data, areas 1 and 4 of this image are replaced with midsection slices of the first and last day in the rotation. The created map best represents each Carrington rotation.

Chapter 4: Results

The new approaches discussed in Chapter 3 were used in this research to investigate sources of discrepancy between traditional means of obtaining the open flux discussed in Chapter 2 (i.e., in situ observations vs. model results). Some questions that were addressed include:

1) Do diachronic versus synchronic PFSS open flux estimates differ significantly from one another?
2) How do open flux estimates based on observational derived coronal holes compare with model and in situ values?
3) Do open flux estimates based on coronal hole observations reveal potential sources for the discrepancy (i.e., found between methods)?

4.1 Diachronic vs. Synchronic Input into WSA

From Chapter 2, Figure 2.5 reveals the periods of discrepancy between model-derived and in situ unsigned open flux since the year 1990. The model-derived results were obtained using traditional diachronic maps as the magnetic

field input. As mentioned previously diachronic maps provide a time history of the Sun's global magnetic field over a Carrington rotation and do not account for well known photospheric flux transport processes. To investigate whether diachronic input maps could result in potential field based models under predicting open flux, synchronic ADAPT maps were used as input into WSA to derive the unsigned open flux. Figure 4.1 shows the results comparing how the two different types of magnetic field input maps affect the model-derived open flux, where each data set is plotted as three Carrington rotation running averages.

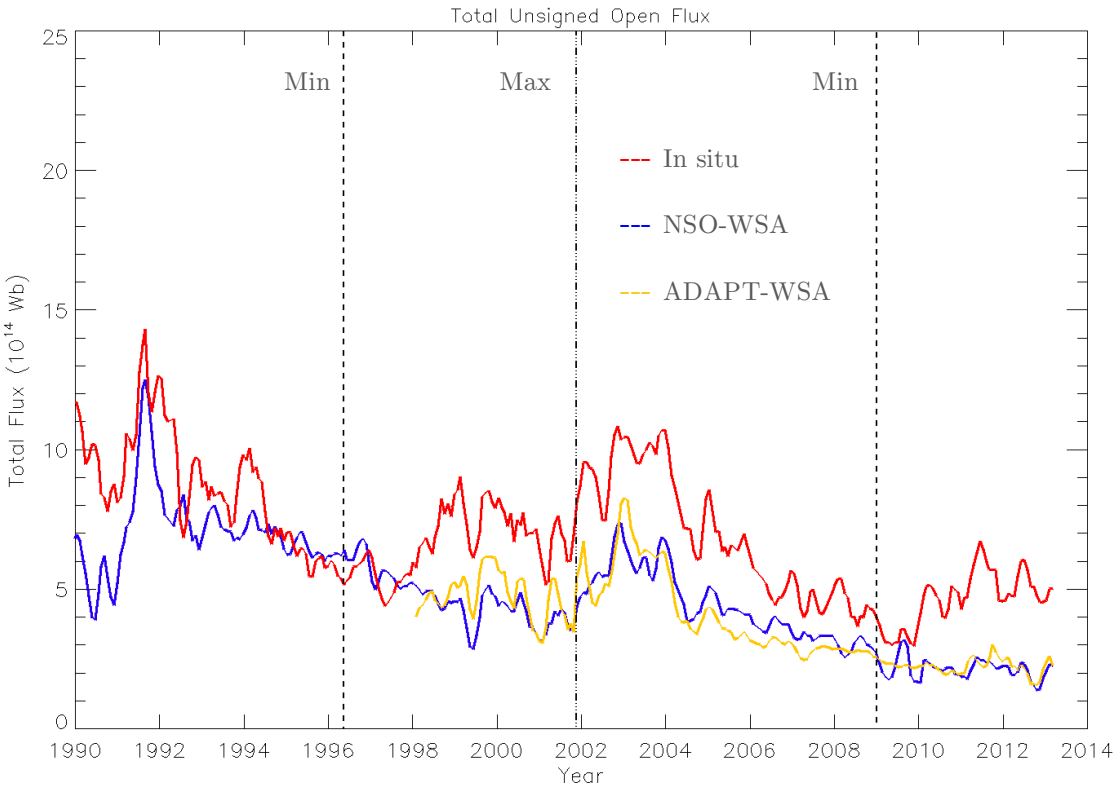

Figure 4.1: Total unsigned open flux (10^{14} Webers) from 1990 to 2013. Specific data sets included in this figure are the OMNI (in situ) data in red, the model-derived open flux using WSA and diachronic inputs maps of the solar magnetic field in blue, and the WSA results using ADAPT synchronic maps as input in yellow. All data shown is plotted as a 3 Carrington rotation running averages. Black dashed lines beginning with solar minimum in 1996 mark periods (left to right) of alternating extremes in solar activity.

The model-derived results using both synchronic and diachronic maps track, on the whole, well with each other for the time period in the previous figure. The WSA-ADAPT results begin in 1998 due to a known calibration issues with the KPVT magnetogram data used to create the ADAPT maps prior to this year. NSO is currently working to resolve the issues. Calibration offsets between different magnetogram sources are known to range from two to as much as five and can present a significant challenge in studies like this. Significant errors can also be introduced when converting raw magnetograms into radial fields to make synchronic and diachronic maps of the field (Riley et al., 2006). However, here both the synchronic and diachronic maps were created using magnetograms from the identical sources (i.e., NSO KPVT and VSM data).

The ADAPT model produces an ensemble of 12 global magnetic field maps where each solution, or realization, varies slightly in magnetic field transport parameters (e.g., north/south meridional flow rates, supergranulation, cell distribution, etc.) based on observational and model uncertainties (see Section 3.1.2). These 12 maps are used as input into WSA for each Carrington rotation. Thus, over a 3 Carrington rotation timeframe, 36 coronal hole maps are created with different calculations of open flux. The standard deviation of the range of variance can then be calculated over these 36 results of open flux. Figure 4.2 differs from Figure 4.1 in that it includes the above described standard deviation for the WSA-ADAPT results.

The standard deviation in the model-derived results using ADAPT maps shows larger spreads during solar maximum compared to periods near solar minimum. During times of solar maximum is where the largest discrepancies occur between model and in situ observations as well. However, there appears to be no dramatic difference between the model-derived open fluxes when two different types of magnetic field input are used. This result shows that varying the magnetic field input into the model does not explain the deviation between the in situ observations and the model-derived open flux.

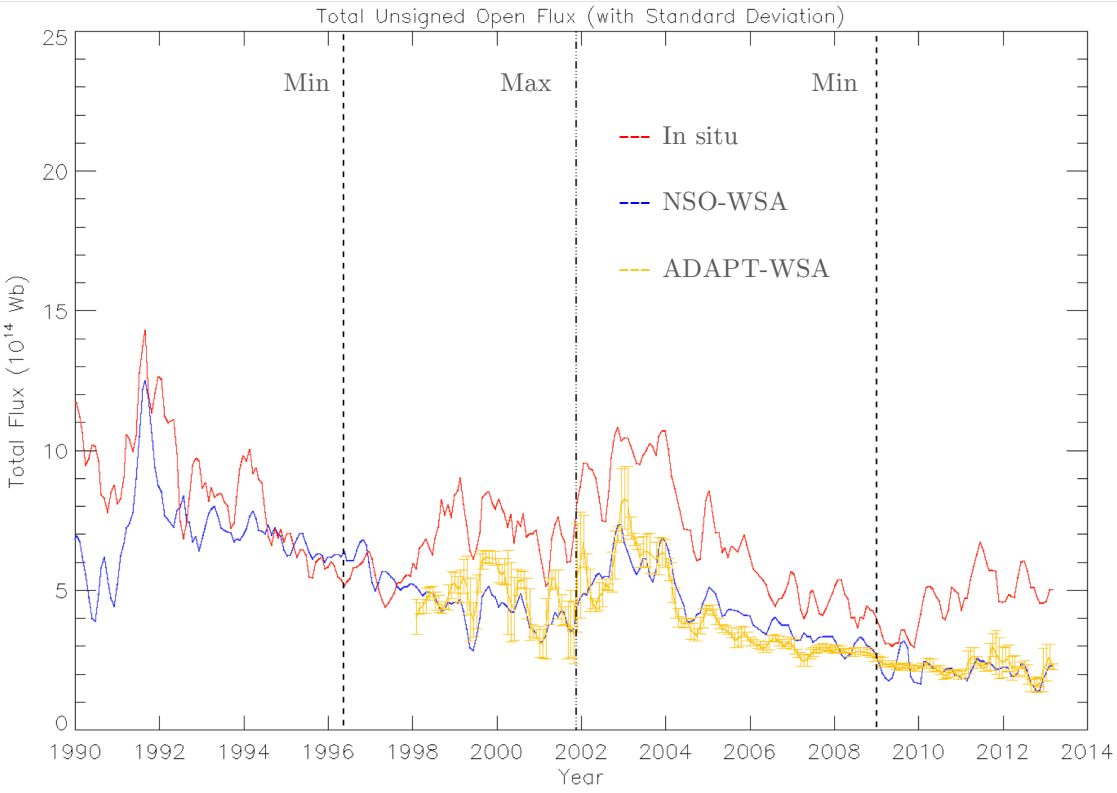

Figure 4.2: Same as Figure 4.1 with the addition of the standard deviation of the ADAPT-WSA results (yellow).

4.2 Open Flux Derived Using Coronal Hole Observations

4.2.1 Coronal Holes Observed in He I 1083 nm Data

The method of using coronal hole observations to calculate open flux was first introduced by Frank Recely and Karen Harvey (2002) (see Section 3.2.1). Using He I 1083 nm spectroheliograms, they manually derived coronal holes and overlaid them onto NSO KPVT diachronic maps of the solar magnetic field to obtain the open flux. An ideal starting point for this research was to compare the open flux results with results generated using models and in situ observations, and then apply the technique to more recent corona images (i.e., EUV data). Figure 4.3 displays the results of using Helium derived coronal holes to calculate open flux (green), and the results (shown previously) using diachronic maps in WSA and in situ observations.

For an 8-year period (1992 – 2000) centered roughly around solar minimum, there is excellent agreement between the open flux calculated from Helium 1083 nm observations (green) and the WSA results (blue). Both methods use diachronic maps to obtain the radial magnetic field, creating a nice comparison. A portion of this time period (approx. 1994 – 1998) is also when the spacecraft data agree with the model-derived values. It is remarkable how well these two results coincide with each other, and suggests that the models capture well the coronal holes identified observationally, at least on a 3-month time scale. Figures 4.1 – 4.3 suggest that the major discrepancy is near solar maximum. For the Helium derived result, the open flux is lower than that obtained with the model for both periods of solar maximum. This could be due to a combination of factors, one of which being the known difficulty of observing coronal holes in Helium at the Sun's mid-latitude region during periods of high solar activity (Arge et al., 2003a). Field strengths from mid- latitude coronal holes can be up

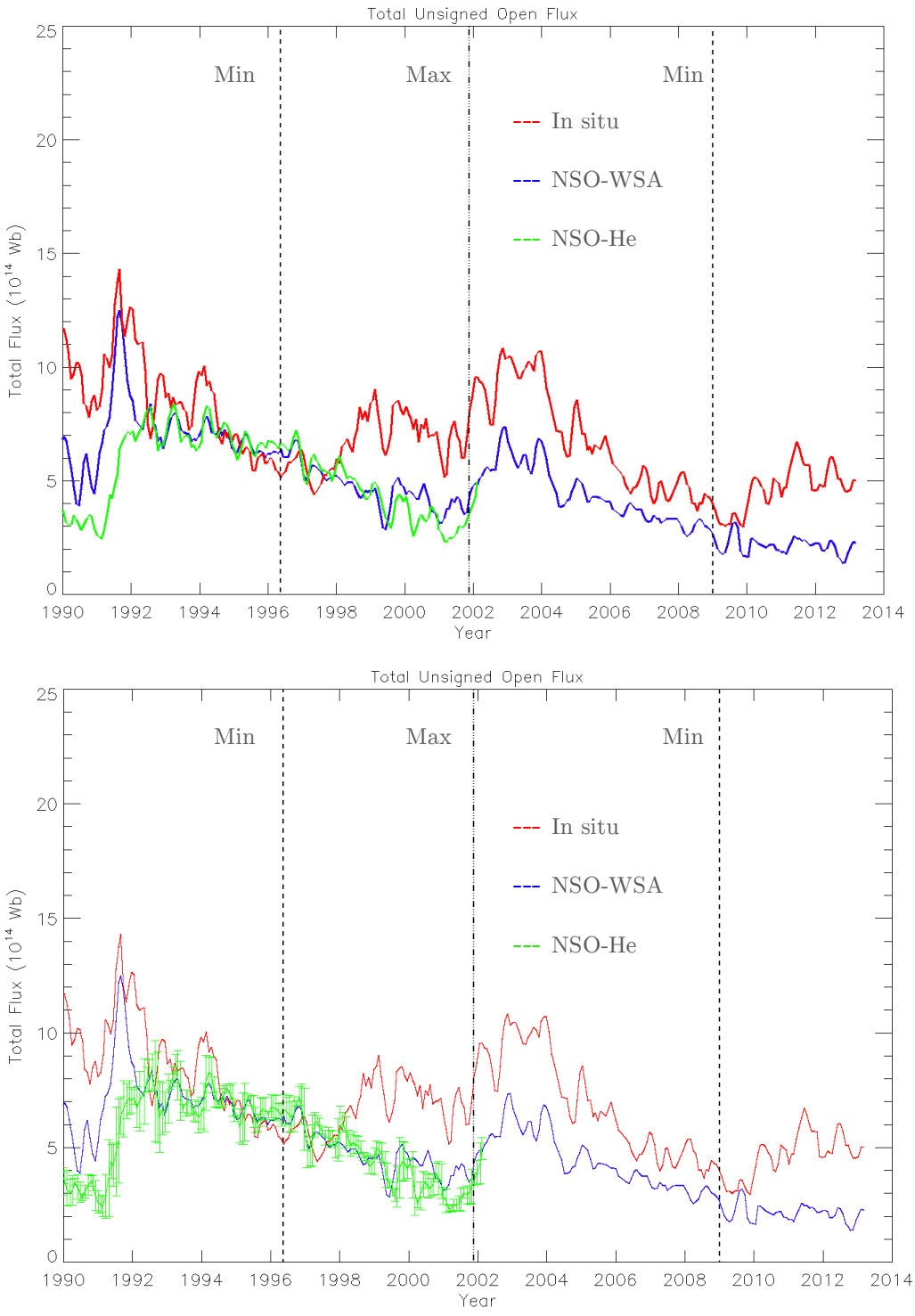

Figure 4.3: a) (top) Total unsigned open flux (10^{14} Webers) from 1990 to 2013 with open flux obtained from observing coronal holes in Helium (green). The in situ data is shown in red, and the open flux derived using WSA and diachronic NSO maps is shown in blue. **(bottom)** Same as Figure 4.3a with the range of variance representing the standard deviation of the Helium derived result.

to four times as strong during solar maximum (Arge et al., 2002). If some of these coronal holes were undetected, it would explain why the Helium derived open flux is lower during these periods.

4.2.1.1 Using ADAPT maps with He Derived Coronal Holes

For a short period of three years, there is an overlap between Helium derived data synchronic ADAPT maps. However, Harvey and Recely identified coronal holes in Helium on diachronic representations of the corona (over a 27 day Carrington rotation) and the ADAPT maps represent the Sun for one particular day. Helium derived coronal holes were overlaid onto the ADAPT map that represented the mid-rotation date of a Carrington rotation to calculate the open flux. This result is shown in Figure 4.4. The comparison can be

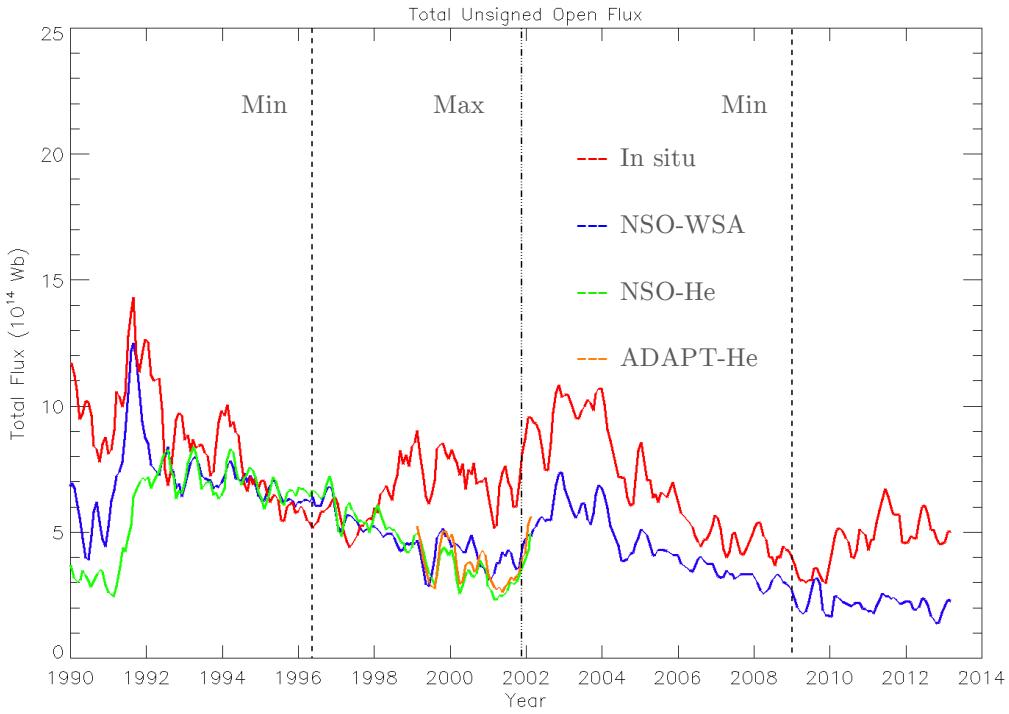

Figure 4.4: Same as Figure 4.3a, with the inclusion of the results using Helium derived coronal holes with ADAPT (orange).

extended back to 1990 once the calibration issues (discussed in Section 4.1) with the NSO KPVT magnetograms used in ADAPT have been resolved. For the short period of overlap, Figure 4.4 shows using both synchronic and diachronic representations of the Sun's magnetic field with observationally derived He coronal holes produce very similar results. This suggests that using synchronic vs. diachronic maps to calculate open flux in this manner makes virtually no difference. In hindsight, this makes sense because while one expects diachronic vs. synchronic maps to differ for any given moment in time, one shouldn't expect significant average differences over three rotation time intervals.

4.2.2 Coronal Holes Observed from EUV Images

Applying a method similar to that used by Harvey and Recely, coronal holes were identified using EUV images of the corona from the NASA STEREO and SDO AIA instruments. Using EUV images is much more desirable because they represent the Sun at one moment in time (see Section 3.2.2) exactly like the maps that the ADAPT model produces. In this way, coronal holes can be identified on a synchronic EUV map and overlaid onto synchronic magnetic field maps to derive the open flux. The results of this technique spanning the years 2007 to 2013 are seen in Figure 4.5.

Similar to comparing model-derived open flux and that surmised through coronal holes observed in Helium, the EUV-ADAPT derived open flux (cyan) follows closely with the model-derived results (blue). This has been the case for all of the results presented thus far and will be discussed further in Section 4.3. There are instances where the two do not exactly match, but overall they are both tracking with each other and separate from the in situ observations. Again, the range of variance is larger outside of solar minimum.

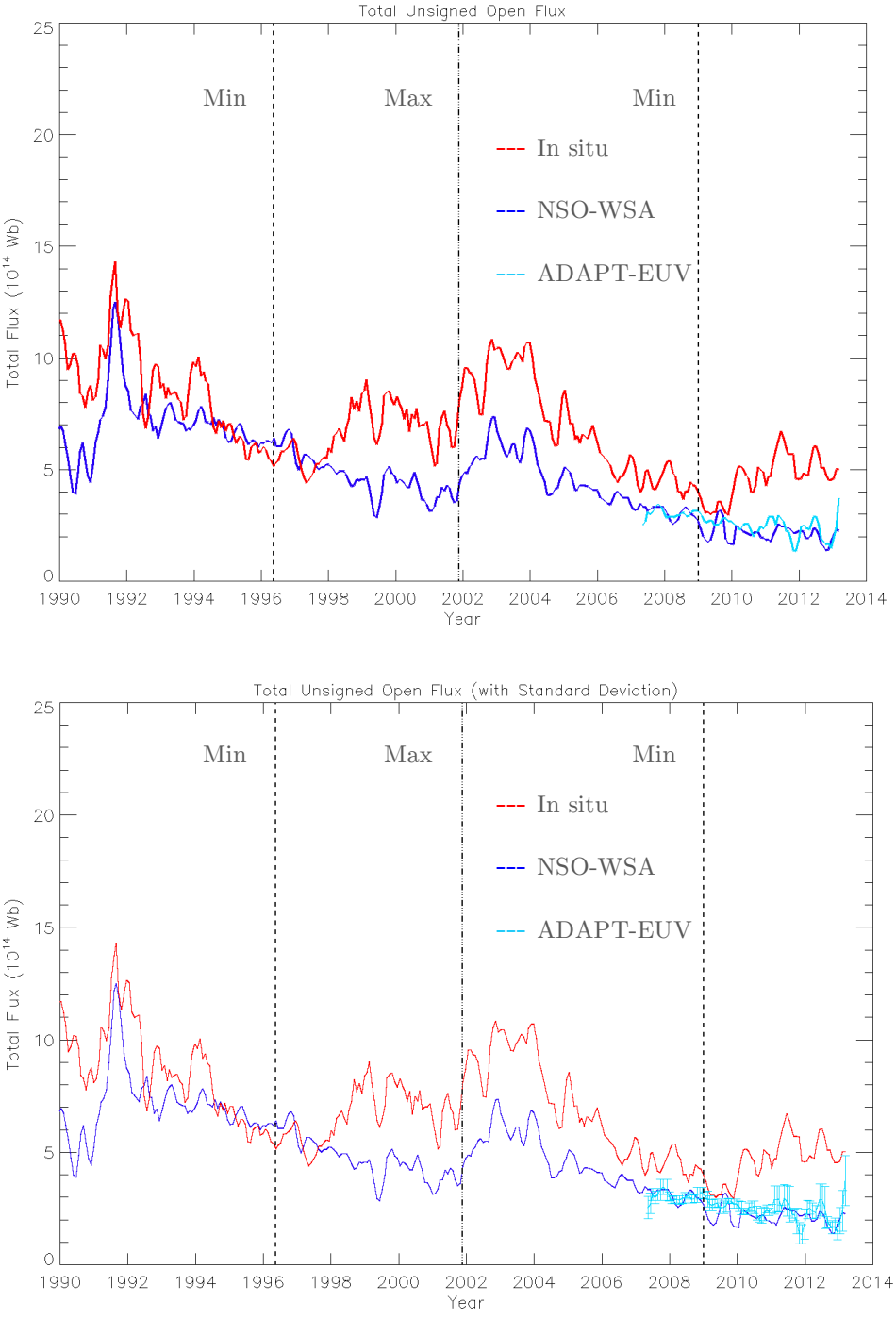

Figure 4.5: a) (top) Total unsigned open flux (10^{14} Webers) from 1990 to 2013 with open flux obtained from observing coronal holes in EUV and pairing with ADAPT maps (cyan). **b) (bottom)** Same as Figure 4.5 a) with the inclusion of range of variance representing the standard deviation of the EUV derived result.

4.3 Discussion of Results

Figure 4.6 displays the unsigned open flux surmised from each technique altogether on one plot. Figures 4.7 and 4.8 show the range of variation for each added data set based on the standard deviation and minimum/maximum values (respectively) over a three Carrington rotation running average. A notable reoccurrence is the agreement between the model-derived open flux, and that surmised using the observationally identifying coronal hole method. On the whole, these two methods provide very similar results. This strongly suggests that potential field based models, such as WSA, are accurately reproducing the global coronal field configuration identified in Helium and EUV observations on a three Carrington rotation time scale.

Further, the in situ observations (red) consistently disagree with the open flux derived from other methods, with the best agreement only near solar minimum. The open flux values as derived by in situ observations are consistently greater than the results of other methods from 1998 onward, with the most deviation occurring near solar maximum. During times of high solar activity, large polar coronal holes weaken and the majority of coronal holes are concentrated in the mid-latitude regions. Currently, the models derive open flux based on the assumption that the main source of open flux is in fact from coronal holes. In reality, near active regions time-dependent magnetic fields are constantly opening and closing in the mid-latitude regions. This could be contributing enough additional open flux to explain why the models under predict open flux compared to in situ observations primarily near solar maximum. Potential field models are unable to account for such time-dependent phenomena when it assumes a steady state solution to the coronal field and only calculates open flux originating from coronal holes. More advanced time-dependent models will be required to address this issue.

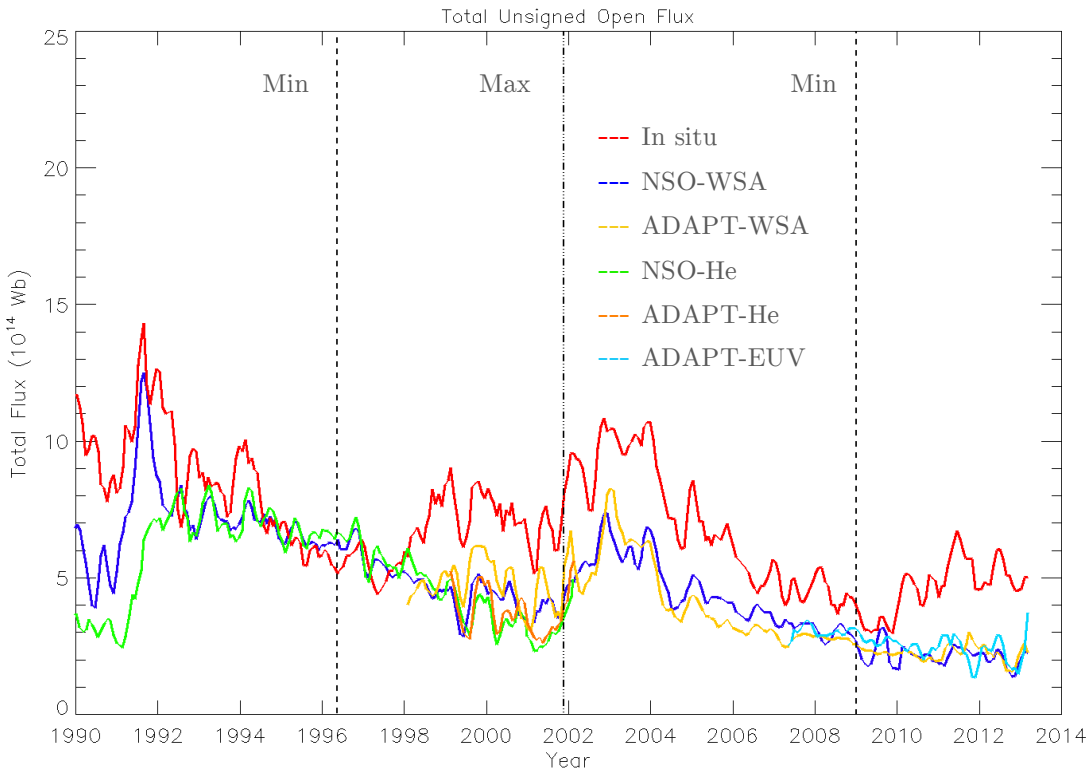

Figure 4.6: Total unsigned open flux (10^{14} Webers) from 1990 to 2013 for all of the aforementioned results. All data are plotted as 3 Carrington rotation running averages. Black dashed lines beginning with solar minimum in 1996 mark periods (left to right) of alternating extremes in solar activity.

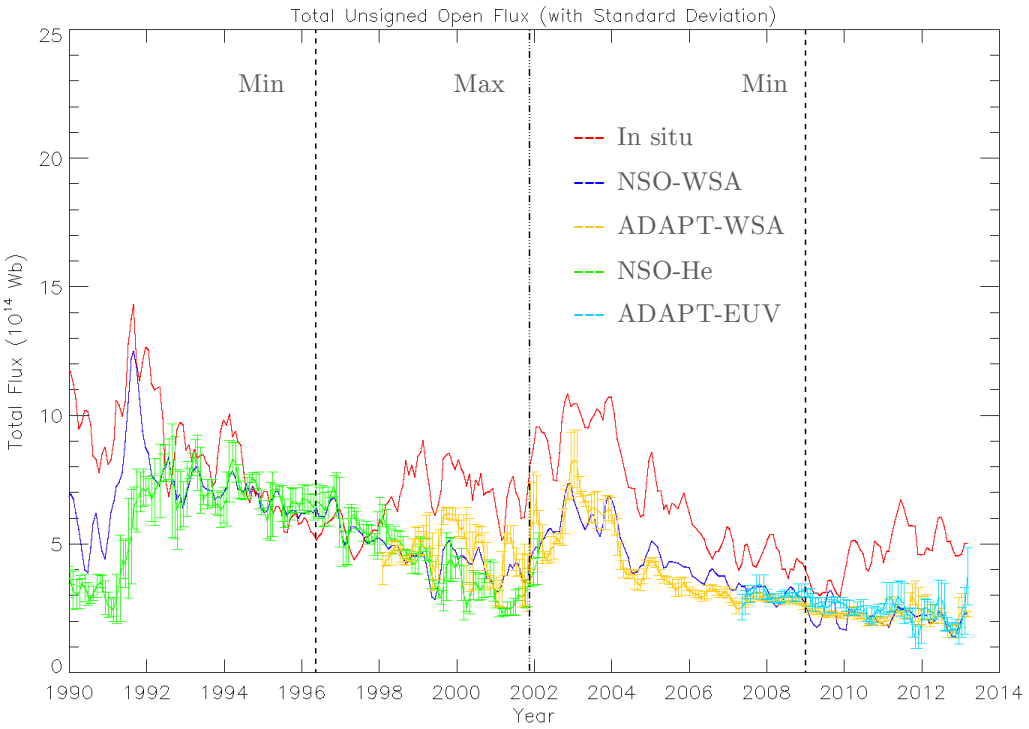

Figure 4.7: Same as Figure 4.6 with the range of variance representing the standard deviation of the results of each new approach.

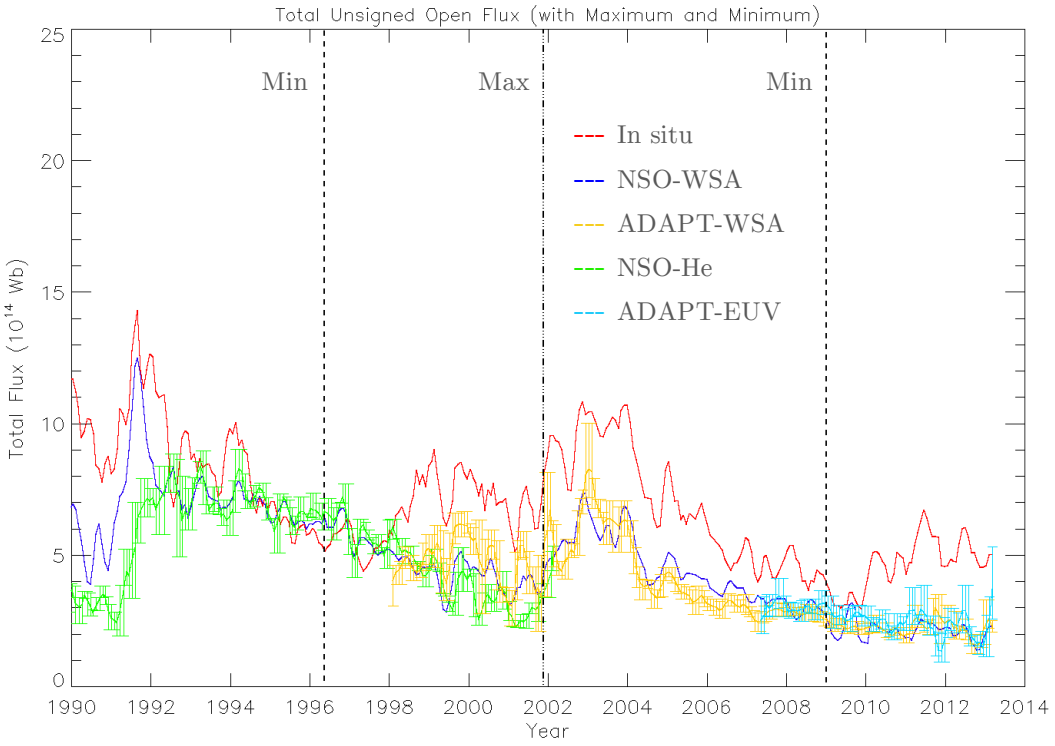

Figure 4.8: Same as Figure 4.6 with the inclusion of the minimum and maximum values of each average, showing the range of variance in the results of each new approach.

The previous discussion is primarily focused on model shortcomings. However, the questions still remain regarding the sources of disagreement between the results of various methods and spacecraft observations. First, in situ spacecraft certainly detect radial components of the magnetic field resulting from CMEs, which are known to still be closed even in passing Earth. Such events are sources of closed flux and would result in overestimates of open flux. This problem will be most severe near solar maximum, when the CME prediction rate is the greatest. This is consistent with the discrepancies seen in these results. A table of near-Earth interplanetary CMEs eruptions (Richardson & Cane, 2013) was used to locate these periods and remove them from the in situ data in attempt to filter out the effects of CMEs. All of the results shown are with CME periods removed including two days before and after an event. It made a small difference, however, CME field lines may be connected back to the Sun for many days (Owens et al., 2008). Moreover, the in situ data is also subject to mistakenly detecting the tangential component of the magnetic field as the field's radial component. This is due to oscillations in the field lines and $\mathbf{B}_\theta$ falling off slower (1/r) than $\mathbf{B}_r$ ($1/r^2$). Thus, the magnitude of $\mathbf{B}_\theta$ will be much larger that $\mathbf{B}_r$ as radial distance from the Sun increases. Oscillations in the field lines result in the tangential component of the field bleeding into the radial component, making the observed open flux higher than it actually is. These results show that this could be happening even for measurements taken inside 2.5 AU.

It is apparent that the in situ observations are subject to much uncertainty. Figure 4.9 shows the same results as Figure 4.7 with the addition of the range of uncertainty in the spacecraft data. They do not depict error bars, but more the measure of variation in the field. This range of variance is over daily measurements of the in situ observed open flux on a 3 Carrington rotation timescale (approximately 90 days worth of data). One would expect the model to capture the average behavior that the in situ data displays. Instead, the model-derived results and results from other methods fall on the lower end of the large range of variance in the spacecraft data.

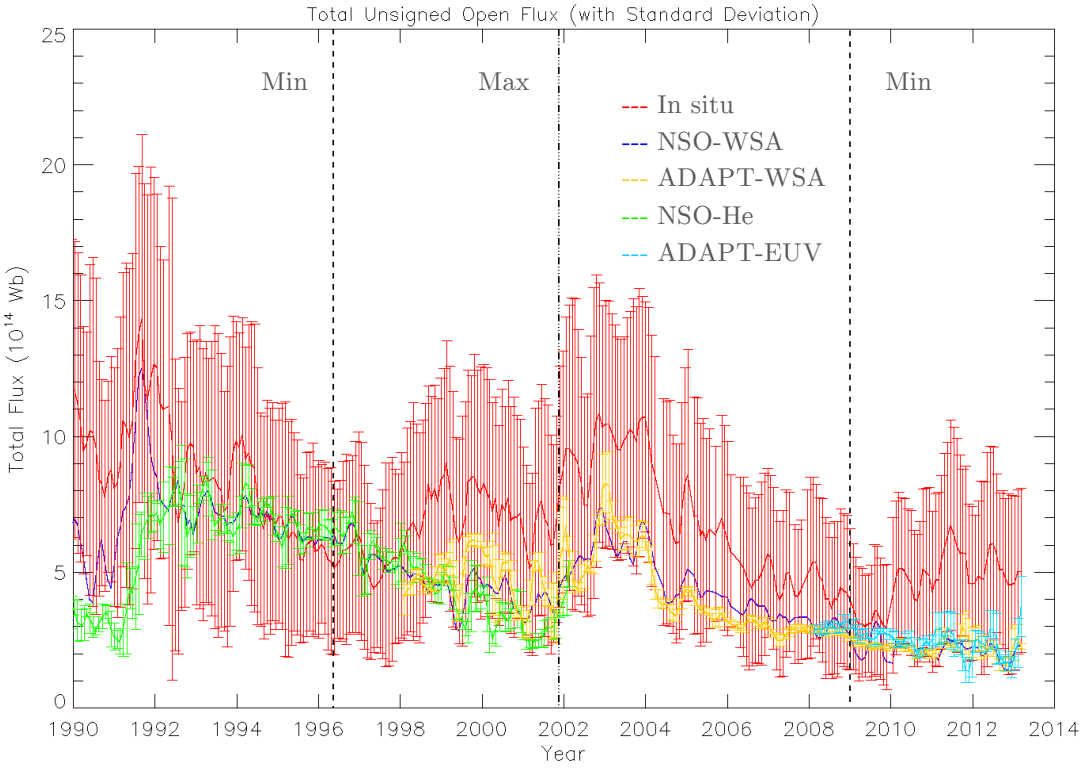

Figure 4.9: Same as Figure 4.7 with the inclusion of the standard deviation showing the range of variance of the in situ observations.

Chapter 5: Concluding Remarks

The motivation of this research was to explore alternative methods for calculating the total unsigned open heliospheric magnetic flux in order to shed light on discrepancies between in situ observations and model-derived open flux. Both data sets of the aforementioned methods have been known to disagree especially in the last decade. Investigating the accuracy of a potential field model to derive the open flux can reveal how well they represent coronal hole boundaries, and thus the true state of the corona for any given time.

One new approach was to use both diachronic and synchronic maps as input into a potential field based model (WSA) and see if any significant differences resulted in the open flux. The diachronic maps, traditionally known as "synoptic" maps, are comprised of NSO KPVT and VSM magnetograms assembled by Carrington rotation. These maps are not truly synoptic, as they cannot represent the Sun's magnetic field at one point in time. More accurately, they represent the solar magnetic field as a time history of the central meridian, thus diachronic. On the contrary, these same magnetograms can be used an input into the ADAPT model to represent the field at one moment in time. The ADAPT model accomplishes this through the use of data assimilation based on observational and model uncertainties. The result is an ensemble solution of 12

synchronic realizations of the field, providing a means to find the standard deviation and show the range of variance. Another approach was to identify coronal holes in He I 1083 nm (diachronic spectroheliograms) and EUV (synchronic representation) emissions to obtain the differential area of open field lines. Then, these coronal hole maps were overlaid onto their respective pairings of magnetic field maps to calculate the open flux.

Major developments from the results included both types of magnetic field representations an input into WSA showing little difference in the model-derived open flux. This is somewhat suspected, as all the results are over a three Carrington rotation running average. The ADAPT model can better represent the Sun's magnetic field on any given day compared to a traditional map from NSO, but when averaged over three Carrington rotations it is not surprising that they produce similar results. Future work will investigate the average field strengths coming from both polar and mid-latitude coronal holes to see how ADAPT handles each compared to using a standard magnetic field map.

Further, the open flux calculated from coronal hole observations in both Helium and EUV tracked well with model-derived results, especially during times surrounding solar minimum. This was encouraging, as it suggests that the WSA model is deriving the coronal hole boundaries and areas accurate to observations of the corona. The most deviation between these two results occurred during solar maximum. The results obtained through Helium observations are consistently lower during solar maximum, potentially due to the known difficulty in observing mid-latitude coronal holes in this emission during periods of high solar activity. As for EUV, there is not enough data to conclusively say that there is greater deviation from the model-derived results during solar maximum. However there are larger ranges of uncertainty outside of solar minimum.

Moreover, the spacecraft data disagrees with all other methods especially during solar maximum. This data is suspect to including closed flux sources from large-scale events (i.e., CMEs), and attempts were made to eliminate those periods. However, CMEs are known to have both endpoints of the field line

attached even near Earth. Thus, the effects they can have on the in situ observations of open flux can be far reaching. Further, the models and coronal hole observation methods could be notably lower than the spacecraft data due to their inability to capture all of the Sun's time-dependent effects. Both operate under the assumption that the main source of open flux is from coronal holes, and do not account for other sources. During solar maximum, the opening and closing of field lines near active regions could contribute enough additional open flux to explain this difference. On the other hand, the spacecraft data could be greater due to instruments mistaking oscillations in the fields' tangential component as the radial component. The in situ data is also highly variable, seen in the standard deviation over three Carrington rotations (Figure 4.9). Model-derived open flux and that obtained through coronal hole observations provide only a static solution. However, one would expect this solution to replicate the in situ results on average, and not just fall within the range of its uncertainty. Thus, the oscillation of field lines is suspected to be a major component to this problem especially given that the models are agreeing with open flux obtained from other approaches.

It is important to determine whether or not spacecraft are accurately representing $\mathbf{B}_r$ for a number of reasons, including the fact that for many decades these measurements have been believed to give the most accurate representation of open flux. Future study will work to eliminate the effects of the tangential component in measurements of $\mathbf{B}_r$ in attempt to resolve some discrepancies. Another motivating factor in improving spacecraft measurements of $\mathbf{B}_r$ near Earth, although not specifically within the focus of this study, is that it would permit a more accurate prediction of the $\mathbf{B}_z$ component of the ambient solar wind impinging on the Earth's magnetosphere. This could lead to improved forecasts of minor to moderate geomagnetic disturbances.

To conclude, the ultimate motivation of this study was to compare in situ observations and model-derived open flux with that surmised from alternative methods. There are obvious discrepancies between model-derived open flux and

in situ observations of open flux. It is not completely clear whether the sources of discrepancy are due to problems within the model itself or with the interpretation of spacecraft observations. Given that the open flux estimates derived from models (i.e., WSA) and that obtained through observationally derived coronal holes show good agreement (except during solar maximum) suggests the possibility that assumptions used to derive global open flux from single point spacecraft measurements of $\mathbf{B}_r$ may be flawed. The latter point will be investigated further in future work.

References

Altschuler, M. D., & Newkirk G., (1969). Magnetic Fields and the Structure of the Solar Corona - I: Methods of Calculating Coronal Fields. *Solar Physics*, 9(1), 131–149.

Arge, C. N., & Pizzo, V. J. (2000), Improvement in the Prediction of Solar Wind Conditions Using Near-Real Time Solar Magnetic Field Updates, *Journal of Geophysical Research*, 105(A5), 10465-10479.

Arge, C. N., Harvey, K. L., Hudson, H. S., & Kahler, S. W. (2003a). Narrow Coronal Holes in *Yohkoh* Soft X-Ray Images and the Slow Solar Wind. *Solar Wind 10, AIP Conference Proceedings*. 202-205

Arge, C. N., Henney, C. J., Gonzalez-Hernandez, I., Toussaint, W. A., Koller, J., & Godinez, H. C. (2013). Modeling the Corona and Solar Wind Using ADAPT Maps that Include Far-side Observations. *Solar Wind 13, AIP Conference Proceedings*. 1539. 11-14

Arge, C. N., Henney, C. J., Koller, J., Compeau, C. R., Young, S., Mackenzie, D., Fay, A., & Harvey, J., W. (2009). Air Force Data Assimilative Photospheric Flux Transport (ADAPT) Model. *Solar Wind 12, AIP Conference Proceedings,* 1216, 343–346.

Arge, C. N., Henney, C. J., Koller, J., Toussaint, W. A., Harvey, J., W., & Young, S. (2010). Improving Data Drivers for Coronal and Solar Wind Models. *Numerical Modeling of Space Plasma Flows, ASP Conference Proceedings*, 444, 99-104

Arge, C. N., Hildner, E., Pizzo, V., J., & Harvey, J. W. (2002). Two Solar Cycles of Nonincreasing Magnetic Flux, *Journal of Geophysical Research*, 107(A10), 1319.

Arge, C. N., Luhmann, L. G., Odstrcil, D., Schrijver, C. J., & Li, Y. (2004). Stream Structure and Coronal Sources of the Solar Wind During May 12th, 1997 CME, *Journal of Atmospheric and Solar-Terrestrial Physics*, 66, 1295 – 1309.

Arge, C. N., Odstrcil, D., Pizzo, V. J., & L. R. Mayer (2003b), Improved Method for Specifying Solar Wind Speed Near the Sun, *Solar Wind Ten*, *AIP Conference Proceedings*, 679.

Babcock, H. W. (1971). The Topology of the Sun's Magnetic Field and the 22-Year Cycle. *The Astrophysical Journal*, 133, 572.

Bennett, J.O., Donahue, M. O., Schneider, N., & Voit, M. (2012). *The Essential Cosmic Perspective* (6^{th} ed.). San Francisco, CA: Pearson Prentice Hall Inc.

Bouttier, F., & Courtier, P. 2002, *Meteorological Training Course Lecture Series, ECMWF*, 1

Bushby, P., & Mason J. (2004). Understanding the Solar Dynamo. *Astronomy and Geophysics*, 45(4), 4.07-4.13.

Cattaneo, F., & Hughes, D. W. (2001). Solar Dynamo Theory: A new look at the origin of small-scale magnetic fields". *Astronomy and Geophysics*, 42(3), 3.18-3.22

de Toma, G., Arge, C. N., & Riley, P., (2005). Observed and Modeled Coronal Holes, *Solar Wind 11*, *AIP Conference Proceedings*, 609-612.

Edlén, B. (1942). Die Deutung der Emissionslinien im Spektrum der Sonnenkorona. Zs. f. Ap. 22, 30–64.

Evenson, G. (2003). The Ensemble Kalman Filter: Theoretical Formulation and Practical Implementation. *Ocean Dynamics*, 53, 343-367.

Griffiths, D. (2012). *Introduction to Electrodynamics (4th ed.)*. Addison-Wesley.

Grotrian, W. (1939). Naturwissenschaften. 27, 214.

Hale, G. E. (1908). On the Probable Existence of a Magnetic Field in Sun-spots. *The Astrophysical Journal*, 28, 315.

Hale, G. E., Ellerman, F., Nicholson, S. B., & Joy, A. H. (1919). The Magnetic Polarity of Sun-spots. *The Astrophysical Journal*, 49, 158.

Harvey, K.L., & Recely, F. (2002). Polar Coronal Holes During Cycles 22 and 23. *Solar Physics*, 211(1-2), 31-52

Hoeksema, J. T., Wilcox, J. M., & Scherrer, P. H. (1983). The Structure of the Heliospheric Current Sheet - 1978-1982. *Journal of Geophysical Research.* 88, 9910-9918.

Hundhausen, A. J. (1995). The Sun and its Magnetohydrodynamics. In M. G. Kivelson & C. T. Russell. *Introduction to Space Physics.* (pp. 91-96). Los Angeles, CA: Cambridge University Press.

Kivelson, M. G. (1995). Physics of Space Plasmas. In M. G. Kivelson & C. T. Russell (1995). *Introduction to Space Physics.* (pp. 50). Los Angeles, CA: Cambridge University Press.

Klimchuk, J. A. (2005). On Solving the Coronal Heating Problem. *Solar Physics*, 234(1), 41-77

Leighton, R. B. (1969). A Magneto-Kinematic Model of the Solar Cycle. *The Astrophysical Journal*, 156, 1.

Linker, J. A., Mikić, Z., Riley, P., Downs, C., Lionello, R., Henney, C. J., & Arge, C. N. (2013). Coronal and Heliospheric Modeling Using Flux-Evolved Maps. *Solar Wind 13, AIP Conference Proceedings*. 1539. 26.

Lockwood, M., Forsyth, R. J., Balogh, A., & McComas, D. J., (2004), Open Solar Flux Estimates From Near-Earth Measurements of the Interplanetary Magnetic Field: Comparison of the First Two Perihelion Passes of the Ulysses Spacecraft, *Annales Geophysicae,* 22, 1395–1405.

Owens, M. J., Arge, C. N., Crooker, N. U., Schwadron, A. & Horbury, T. S. (2008). Estimating Total Heliospheric Magnetic Flux from Single-point In Situ Measurements. *Journal of Geophysical Research*, 113(A12), A12103.

Parker, E. N. (1955). Hydromagnetic Dynamo Models. *The Astrophysical Journal*, 122, 293.

Parker, E. N. (1958). Dynamics of the Interplanetary Gas and Magnetic Fields. *The Astrophysical Journal*, 128, 664

Pattichis, M. S., Jatla, V., Hock, R. A., Henney, C. J., & Arge, C. N. (2014). Detecting Coronal Holes for Solar Activity Modeling, *Asilomar Conference on Signals, Systems and Computers*.

Priest, E. R. (1995). The Sun and its Magnetohydrodynamics. In M. G. Kivelson & C. T. Russell. *Introduction to Space Physics*. (pp. 58 – 61). Los Angeles, CA: Cambridge University Press.

Riley, P., Linker, J. A., Mikić, Z. & Lionello, R. (2006). A Comparision Between Global Solar Magnetohydrodynamic and Potential Field Source Surface Model Results. *The Astrophysical Journal*, 653, 1510-1516.

Schwabe, H. (1843). Solar Observations During 1843. *Astronomische Nachrichten*, 20, 495.

Schwarzschild, M. (1948). On Noise Arising from the Solar Granulation. *The Astrophysical Journal*, 107, 1

Shatten, K. H. (1971). Current Sheet Magnetic Model for the Solar Corona. *Cosmic Electrodynamics*, 2, 232-245

Shatten, K. H., Wilcox, J. M., & Ness, N. F. (1969). A model of interplanetary and coronal magnetic fields. *Solar Physics*, 6(3), 442-455.

Smith, E. J., Balogh, A., Forsyth, R. J., & McComas, D. J., (2001). Ulysses in the south polar cap at solar maximum: Heliospheric magnetic field. *Geophysical Research Letters*, 28(22), 4159-4162.

Sturrock, P. A. (1999). Chromospheric Magnetic Reconnection and Its Possible Relationship to Coronal Heating. *The Astrophysical Journal*, 521, 451-459.

Wang, Y.-M., Sheeley, N. R., Jr. (1992). On Potential Field Models of the Solar Corona. *The Astrophysical Journal*, 392(1), 310-319.

Worden, J. & Harvey, J., (2000). An Evolving Synoptic Magnetic Flux Map and Implications for the Distribution of Photospheric Magnetic Flux. *Solar Physics*, 195(2), 247-268.